NANOPHOTONIC TECHNOLOGIES FOR MANIPULATING BIOMOLECULES AND INVESTIGATING MOLECULAR INTERACTIONS

A Dissertation

Presented to the Faculty of the Graduate School

of Cornell University

In Partial Fulfillment of the Requirements for the Degree of

Doctor of Philosophy

by

Pilgyu Kang

August 2014

NANOPHOTONIC TECHNOLOGIES FOR MANIPULATING BIOMOLECULES AND INVESTIGATING MOLECULAR INTERACTIONS

Pilgyu Kang, Ph.D.

Cornell University 2014

ABSTRACT

This dissertation aims to develop nanophotonic technologies by integrating photonic-crystal-based nanostructures with microfluidic techniques. Firstly, a self-assembled photonic nanostructure is developed to exploit that a range of colors on incident light will reflect on a crystalline structure with appropriate periodicity. The photonic crystal substrates are utilized to demonstrate a technique for creating erasable, high-resolution color images with transparent inks.

The photonic-crystal-based technique is applied to construct a photonic crystal resonator in the waveguide through which light travels and is confined in small mode volume. The confined light energy enables the optical force experienced by a trapped dielectric nanoparticle. Based on this principle, angular orientation and rotational control of both biological and non-biological nanoscale rods are demonstrated using a photonic crystal nanotweezer to extend the capabilities of near-field optical techniques, including trapping, transport, and handling of nanomaterials. In experiments, single microtubules (diameter 25 nm, length 8 μm) and multi-walled carbon nanotubes (outer diameter 110 – 170 nm, length 5 μm) are rotated by the optical torque resulting from their interaction with the evanescent field emanating from these devices. An angular

trap stiffness of k = 92.8 pN nm/rad^2-mW is demonstrated for the microtubules and a torsional spring constant of 22.8 pN nm/rad^2-mW is measured for the nanotubes.

Finally, the near-field optical technique is utilized to develop a label-free method for measuring the binding affinity and stoichiometry of free-solution interactions between antibodies and single influenza viruses at the attogram scale. Common approaches, including optical, electrochemical, and mechanical detection schemes require immobilizing one or both of the interacting molecules on an assay plate or a sensor surface, which constrains their active binding. This restriction prevents a precise measurement of their affinity and binding capacity, especially when one of the interacting biomolecules is much larger than the other and multivalent, for example a virus and an antibody. The method, however, presented here detects specific binding by analyzing changes in the confined Brownian motion of the virus, which is trapped but not immobilized using a photonic crystal resonator.

BIOGRAPHICAL SKETCH

Pilgyu Kang earned a Bachelor of Science degree in Mechanical Engineering with a minor in Electrical Engineering at Seoul National University. He received a Master of Science degree in Mechanical Engineering in 2009 at Carnegie Mellon University. In 2009, he joined the doctoral program in Mechanical Engineering at Cornell University.

While pursuing his degree, he worked as a research assistant in Erickson lab and a teaching assistant for the Sibley School of Mechanical and Aerospace Engineering. He has presented his research at international conferences, including Micro-Total Analysis Systems (MicroTAS): The International Conference on Miniaturized Systems for Chemistry and Life Sciences, and the Biophysical Society's (BPS) Annual Meeting. Additionally he has published his research in international journals, including *Langmuir* and *Nano Letters*.

Pilgyu Kang's dissertation, "Nanophotonic technologies for manipulating biomolecules and investigating molecular interactions," was supervised by Dr. David Erickson. In the short term, he looks forward to beginning work as a post-doctoral fellow to gain experiences outside the current field of studies.

ACKNOWLEDGMENTS

This dissertation could never have been accomplished without the help, support, and guidance of a number of people. First of all, I sincerely appreciate my advisor, Dr. David Erickson, for instilling the necessary qualifications I needed to become an independent research scientist. With his support, encouragement, and insightful discussions, I was able to complete my doctoral studies while solving challenges in my research. He always encouraged me to persevere when I was struggling with challenges and waited with patience until I could ascertain solutions for myself. He is a great advisor who encouraged me to think more independently about my experiments and results.

I also would like to thank Dr. Manfred Lindau, one of my committee members, for his insightful discussions. He always welcomed me for discussions by video conference, even when he was abroad for his own research. In addition, I would like to offer my sincere thanks to Dr. Peng Chen for his collaborative research support, as well as his genuine advice on pursuing an academic career.

In addition, I am also thankful for funding opportunities awarded by the the Air Force Office of Scientific Research and the US National Science Foundation, the U.S. Department of Energy Office of Basic Science, and the NIH. I appreciate their resources and the facilities that enabled my research on the fabrication of devices. I am also indebted to the Cornell NanoScale Facility and the Nanobiotechnology Center (NBTC). Finally, I would like to extend my appreciation to Dr. Eric Richards of the Boyce Thompson Institute for Plant Research at Cornell for allowing me to use their resources in my work.

I would also like to thank past and present members of the Erickson lab, especially Dr. Xavier Serey and Dr. Michael Mak, for their assistance with learning techniques and physics when conducting experiments. They provided valuable suggestions at each obstacle I encountered and their willingness to discuss solutions was invaluable. Special thanks to Dr. Aram Chung for his encouragement and helpful advice at the Erickson lab. I would also like to thank other members, including Dr. Yih-Fan Chen, Dr. Mekala Krishnan, Dr. Erica Jung, Dr. Inhee Choi, Dr. Yun Suk Huh, Abdurrahman Gumus, Dr. Bernardo Cordovez, Dr. Li Jiang, Dr. Mattew Mancuso, Dr. Vlad Oncescu, Perry Schein, and Dakota O'Dell for their help and suggestions.

Most importantly, my sincere thanks and deepest love to my family for their constant support, especially my wife Mirae who is always at my side offering encouragement whenever I struggle with frustration. She has also motivated me on many occasions while we have pursued our PhD studies journey together.

TABLE OF CONTENTS

LIST OF FIGURES

CHAPTER 1

INTRODUCTION

1.1 Motivation

Since Ashkin first introduced an optical tweezer in 1970[1], researchers have exploited the tool for studies on a wide range of biological systems by directly manipulating biomolecules, for example holding and moving them. Optical tweezers enabled manipulation at the single particular level such as a single protein or a DNA particle (D ~ 10 nm). Optical manipulation allows for a non-obstructive method to study complex biological systems, especially at 1064 nm wavelength of the light. Despite the usefulness, optical tweezers are restricted from handling a wide range of objects due to the diffraction limit, wherein a laser beam is tightly focused through optical lenses. Thus conventional optical tweezers can barely handle nanoscale objects below 100 nm in diameter because optical force is proportional to radius cubed.

Near-field optical techniques, however, have shown the capability to trap nanomaterials, such as polymer beads, quantum dots, and viruses in sizes as tiny as tens of nanometer diameter. Near-field approaches use resonant recirculation on nanostructures designed to confine light to small volumes. The tighter light confinement allows increased field intensity and sharper field gradient, leading to a large optical trap force expressed as $F_{trap} = 2\pi\alpha\nabla I_0/c$, where α is polarizability of a trapped particle, I_0 is light field intensity, and c is the speed of light[2,3]. Given the large trap force and the manipulation techniques, near-field-based optical techniques have demonstrated a wide range of applications, such as nanoassembly[4-6], biological sensors[7,8], and single molecule analysis[9,10].

These capabilities can be further developed into new technologies through the integration of near-field optical systems with microfluidic techniques. The integrated system is not limited to carrying out tasks like trapping/release and transport, but extended to orient a trapped particle of a rod-like shaped object by a polarized electric field. The added performance can contribute to synthesize nanoscale complex assemblies along with microfluidic controllability of nanomaterials in aqueous condition. The complex assemblies made of biological materials possibly carry out the tasks for target drug delivery[11].

In addition, the integrated systems of nanophotonics techniques and microfluidics techniques can create a new method of monitoring molecular interactions. Existing optical techniques[8,12,13] detect a shift in the distinctive frequency at which electromagnetic energy resonates in specially designed nanostructures for recognizing molecular bindings. Current approaches[14-16] require restricting one of the interacting molecules from interacting with the device surface, or labeling either or both of the molecules with a fluorophore in order to detect the binding of the partner molecules. In this regard, a new approach is desired to measure the interactions conveniently and accurately without the need of immobilization or labeling. Particularly, a novel method is needed for measuring multivalent binding[17], for example, interactions between a large molecule and relatively smaller partner molecules like virus and antibody.

1.2 Goals

There are several goals of the research projects presented here: 1) To develop a colloidal photonic crystal structure and demonstrate its applications, 2) to develop a near-field-based optical manipulation technique of angular orientation control, 3) to study non-linear optics using FDTD simulation in order to obtain a photonic-crystal-based optical resonator and nanofabrication of photonic crystal resonator chips, and 4) to establish a label-free method of measuring molecular interactions between biomolecules using a nanophotonic tweezer based on the nanomanipulation approach and microfluidic techniques.

1.2.1 Aim 1: Colloidal photonic crystal structure via a self-assembling technique

A simple self-assembling technique is used to fabricate a colloidal photonic crystal substrate. The fabricated colloidal photonic crystal substrate shows a potential application as a reflective display since it reflects a specific range of visible wavelength to incident light. In addition, the microfluidic infusion technique locally instills transparent inks into the substrate, which demonstrates the application of a writable display in multicolor images with resolution to 200 μm. Furthermore the image is erased with the same kind but low vapor pressure silicon oil to obtain reusability.

1.2.2 Aim 2: Nanomanipulation technique of angular orientation control

Angular orientation and rotation control of nanomaterials have been demonstrated to extend the capabilities of near-field-based optical manipulation

techniques, including trapping/release and transport. A Transverse Electric (TE) - polarized electric field traveling transversally in a resonant waveguide orients rod-like dielectric materials in parallel to the polarized direction, for example microtubules ($L \approx 8 – 10$ μm and $D \approx 25$ nm) and multi-walled carbon nanotubes ($L \approx 5$ μm and $D_{outer} \approx 110 – 170$ nm). Angular trap stiffness is measured for both materials respectively and the optical torque that can be applied to dielectric materials is calibrated with the angular stiffness for nanophotonic tweezers.

1.2.3 Aim 3: Design of a photonic crystal resonator and nanofabrication

A photonic crystal resonator is designed by the finite-difference time-domain (FDTD) simulation based on the non-linear optics study. The specific goal here is to re-circulate electromagnetic waves between two photonic crystal mirrors that are facing each other, thereby constructing resonance in the optical cavity. . The deterministic design method[18] is used to decide the geometries of the photonic crystal mirror, including diameter and periodicity of holes as well as the cavity length between the mirrors. The designed photonic-crystal-based optical resonator is fabricated with nanofabrication processes, including electron beam lithography and soft lithography.

The photonic crystal resonator has resonance in the cavity at 1064 nm wavelength where it manipulates biological materials nondestructively due to low absorption of heat by optical power. Relatively high transmission is the result of low scattering loss and will generate peak power at the resonance, mainly due to the

smaller number of cavity holes employed in the design. Larger light intensity leads to large optical trap force, despite the deteriorated quality factor.

Common optical detection schemes rely upon high quality factor that allows better sensitivity to detect the change of distinctive resonant frequency. The change results from a small adjustment in the refractive index caused by molecules binding to partner molecules that are immobilized to the surface of the resonator. Immobilization techniques have enabled functionalization of a device for the detection of a specific target, but a convenient molecular detection method has been needed such that the functionalization process can be avoided. The following objective is to develop a novel method that measures molecular interactions accurately and conveniently.

1.2.4 Aim 4: A nanophotonic method of label-free measurement of molecular interactions

The final goal is to develop a nanophotonic detection method of freely interacting biomolecules based on nanomanipulation of single particles and microfluidic techniques. The label-free method developed here measures the binding affinity and stoichiometry of free-solution interactions between antibodies and single influenza viruses at the attogram scale. Existing methods[8,12,13] have relied upon immobilizing one of the interacting biomolecules or labeling either or both biomolecules. In contrary, the approach presented here employs a photonic crystal resonator for a near-field optical trapping of a single virus particle, enabling the detection of specific binding of antibodies by analyzing changes in the confined Brownian motion of the virus. Thus the detection scheme does not require extra

equipment like an optical spectrum analyzer in addition to rendering the immobilization or labeling process unnecessary.

The following chapters discuss how these goals are implemented in greater detail. Prior to the discussion, an overview of related technology and physics, including photonic crystals, photonic-crystal-based resonator, and principles of near-field optical trap of dielectric particles is presented briefly.

Chapter 2

BACKGROUND: PHOTONIC CRYSTALS AND RESONATORS

2.1 Photonic crystals

Photonic crystals have been employed to control light propagation and confine light in a nanostructure. A periodic arrangement of differing dielectric materials forms a periodic potential to propagating electromagnetic wave of light. The constructed photonic crystal systems either pass or reject a certain range of wavelength to form photonic band gaps. Modes refer to wavelengths allowed to travel and bands refer to sets of allowed modes. In this regard, photonic band gaps[19] refer to the disallowed bands of wavelengths. Thus the design of photonic crystal systems allows optical control and manipulation of the flow of light.

The optical modes that photonic crystal systems support are accounted for by solving Maxwell's equations in a periodic dielectric nanostructure, but a practical computational technique, such as the finite domain time difference method, is used to engineer photonic crystal systems. The engineered system constructs a photonic crystal resonator by placing a defect, known as an optical cavity, between the two photonic crystal mirrors.

2.2 Photonic crystal resonators

Light transported through waveguide structures can be localized by defects introduced in photonic crystal mirrors and thereby confined to the defect regions. The field intensity of the trapped light is enhanced in the optical cavity, providing strong

light-matter interactions that enable the optical trapping of dielectric materials whose size range from a few micrometers to tens of nanometers.

An optical resonator confines light to small mode volumes by resonant recirculation. This principle is similar to the Fabry-Perot cavity, formed between two Bragg mirrors, in which light interfering with each other constructively forms a standing wave. On the other hand, photonic crystal waveguides function similarly to the Bragg mirror such that a narrow range of wavelengths is transmitted into the optical cavity to resonate at the peak of designed wavelength. The following section discusses the principle of optical trap of a dielectric particle.

2.3 Principle of nanophotonic trapping using a photonic crystal resonator

2.3.1 Overview of optical manipulation techniques

In 1970, Ashkin introduced the concept of an optical tweezer that traps polystyrene particles of a few micrometers in diameter using a focused Gaussian beam [1]. Later in 1987, Ashkin and colleagues demonstrated optical manipulation of biomolecules, such as viruses and bacteria, for the first time[20,21]. Since then, optical tweezers have been a useful tool to study biological systems thanks to their capability of handling a dielectric particle of varying size from a few micrometers to tens of nanometer. Optical trap force arises from the gradient force, which is proportional to the spatial gradient of light intensity in a beam focus and acts to the direction of high intensity as shown in Figure 2.1. The gradient force is expressed as

$$\vec{F}_{grad} = \frac{\alpha}{2\varepsilon_0 c}\vec{\nabla} I(\vec{r}) \tag{1}$$

where α is the polarizability of a particle, I is the light intensity, ε_0 is the vacuum permittivity, and c is the speed of light. The beam focus is diffraction limited, however, since the focus is implemented by objective lenses.

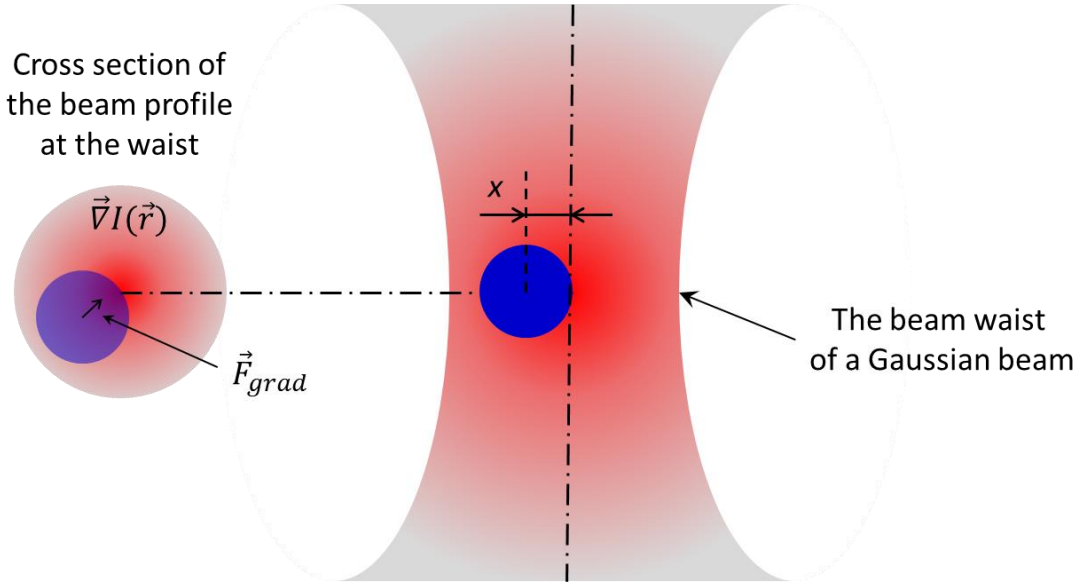

Figure 1 Optical trapping of a particle with a Gaussian beam. The Gaussian beam is focused with objective lenses, resulting in the diffraction limited focus at the beam waist. The gradient force is generated by spatial variation of intensity that has high intensity at the center and becomes lower outward. The magnitude of the gradient force is proportional to that of the gradient, $|\partial I/\partial r|$, and its direction is toward high intensity at the center.

In the diffraction-limited systems, relatively high power ranging from tens of milliwatts to one watt is needed to form stable trap potentials for Rayleigh-sized biological molecules[22] ($d << \lambda$). The high power induces optical damage to biological materials. It also gives rise to thermal excitation of the medium, for example water, by

absorbed optical energy that is transmitted to water. This problem is alleviated by working with a 1064 nm wavelength where a low absorption of light is exhibited[22]. Yet the restriction on Rayleigh-sized biomolecules has been challenging to optical manipulation, especially for biophysics studies at a single molecular level, for example DNA and proteins.

2.3.2 Principle of near-field-based optical manipulation using an optical waveguide

Near-field-based optical manipulation techniques have provided solutions to the restrictions that result from the diffraction-limit. Plasmonic-based techniques[23-25] and optical resonators[8,18,26,27] utilize light's ability to be localized in nanostructures. More specifically, optical resonators based on waveguide structure exploit the exponentially decaying electromagnetic wave field that travels through the waveguide. The evanescently decaying field is formed to high intensity field of light in the vicinity of the structure and low intensity field away from the structure, resulting in gradient force. The gradient force resulting from the evanescent field is expressed as

$$F_{grad} = \frac{2\pi\alpha}{c}\nabla I_o(z) \qquad (2)$$

where α is polarizability of a trapped particle, I_o is incident light field intensity on the trapped particle, and c is the speed of light[2,3,28]. The equation (2) is equal to the equation (1). Note that the equation (2) is in the CGS unit whereas the equation (1) is in the MKS unit. Dielectric particles are pulled down and trapped by the gradient force when they approach the waveguide structure.

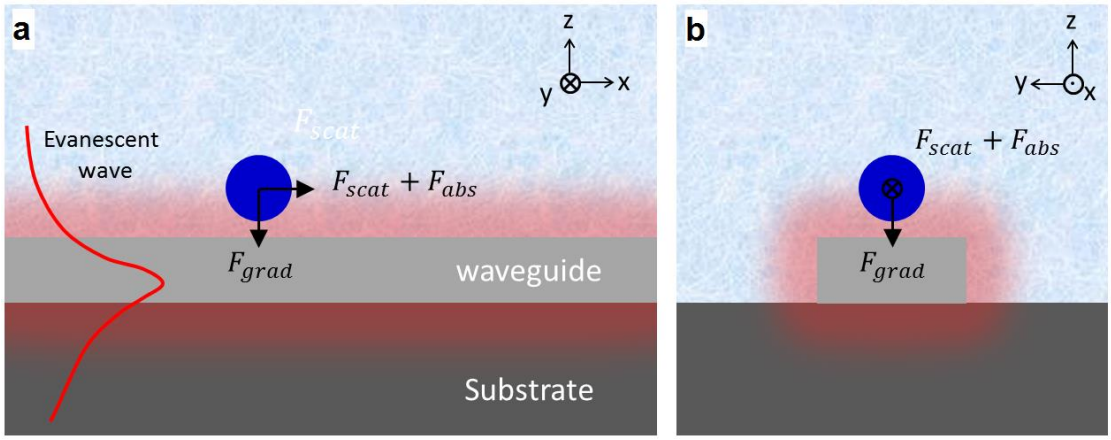

Figure 2 Schematics of a waveguide and radiation forces acting on a Rayleigh particle. The forces are decomposed to two components. One is gradient force acting in the transverse direction of z. The other is propulsive forces including scattering force and absorption force acting in the propagation direction of electromagnetic wave of light. The evanescently decaying field, simply called evanescent wave, is formed in the waveguide structure, allowing the gradient force.

The polarizability, α, of the particle is expressed as $\alpha = 3V(\varepsilon_p - \varepsilon_m)/(\varepsilon_p + 2\varepsilon_m)$, where $V = (4\pi/3)r^3$ is the volume of the particle for a spherical particle, ε_p is the permittivity of the particle, ε_m is the permittivity of the surrounding medium[22]. The permittivity of the particle is a complex value to be expressed as $\varepsilon = \varepsilon' + i\varepsilon''$, relating to the real and imaginary part of the refractive index, n and k respectively, by $\varepsilon = (n + ik)^2$. Given that an imaginary value of refractive index, k, of dielectric materials[2,22] is close to 0, it is noted that $\varepsilon \approx n^2$. Thus the polarizability of a lossless dielectric particle is reduced to be $\alpha = 4\pi r^3(n_p^2 - n_m^2)/(n_p^2 + 2n_m^2)$ that shows dependency of the third power of particle's radius.

In addition, other components of optical forces exist, including scattering force and absorption force, which act upon the direction of wave propagation. The scattering force and the absorption force are expressed as

$$F_{scat} = \frac{8\pi^3 n_{eff}^{\ 5} |\alpha|^2}{3c\lambda^4} I_o \quad (3)$$

$$F_{abs} = \frac{2\pi\varepsilon_m \alpha''}{c\lambda} I_o \quad (4)$$

where I_o denotes the mode intensity in the waveguide when the particle is incident, n_{eff} denotes the effective index of the mode in the waveguide, and α'' denotes the imaginary part of polarizability of the particle provided that the complex polarizability of the Rayleigh particle is defined as $\alpha = \alpha' + i\alpha''$ with real and imaginary parts of the polarizability, α' and α'' respectively, and the rest of parameters are noted as previously[2,3].

These two propulsive forces are opposing forces that impede optical confinement of a trapped particle along the waveguide. On the other hand, a localized field formed in a photonic crystal resonator offers a completely three dimensional optical trap similar to traditional optical tweezers. The localization of light forms a hot spot where the field gradient becomes sharper in a small cross sectional area on the resonant waveguide. A larger spatial gradient provides increased gradient force that confines a trapped particle in the x and y direction, whereas the gradient force resulting from the evanescent field confines the trapped particle in the z direction.

Chapter 3

HIGH RESOLUTION REVERSIBLE COLOR IMAGES ON PHOTONIC CRYSTAL SUBSTRATES

3.1 Abstract

When light is incident on a crystalline structure with appropriate periodicity[29] some colors will be preferentially reflected. These photonic crystals[19] and the structural color[30] they generate represent an interesting method for creating reflective displays and drawing devices since they can achieve a continuous color response and do not require back lighting[31,32]. Here we demonstrate a technique for creating erasable, high-resolution, color images using otherwise transparent inks on self-assembled photonic crystal substrates[33]. Using inkjet printing[34] we show the ability to infuse fine droplets of silicone oils into the crystal, locally swelling it and changing the reflected color. Multi-color images with resolutions as high as 200 μm are obtained from oils of different molecular weights with the lighter oils being able to penetrate deeper, yielding larger red shifts. Erasing of images is done simply by adding a low vapor pressure oil which dissolves the image returning the substrate to its original state.

3.2 Introduction

Structural color is ubiquitous in nature and can be found in butterfly wings[35,36], squid skin[37,38], peacock feathers[39,40] and the spines of sea mice[41]. These animals use structural color and their ability to mechanically change the local periodicity of the internal nanostructures that generate it to create adaptive camouflage[37] or look more

attractive to the opposite sex[39]. Its success in nature has inspired the incorporation of structural color into numerous technologies including displays[31], tunable optical filters[42] and gas sensors[43]. For these and other applications, numerous methods have been developed for tuning structural color including: electrical actuation[44], chemical stimulus[32], light-triggered liquid crystals[45], vapor absorption[46], nanofluidics[47] and mechanical strain[48].

Structural color is a natural fit for new display technologies and writing substrates since it can provide vivid colors in environments of high intensity light (*e.g.* sunlight) without the need for additional illuminating power. Most existing display technologies such as LCDs and LEDs require power to actively project colors and often suffer from performance degradations in these reflective environments. Recognizing this, researchers have developed a number of techniques for dynamically and spatially modulating the colors reflected off of photonic crystal-like substrates, for example, using electrical[31] and magnetic[49,50] actuation methods. The application of these external fields to drive the color change can be fast and provide good dynamic range but they require external power, an embedded method for spatially modulating the field, and are not directly applicable to writing substrates. Here we demonstrate an electrical-power-free infusion technique that allows us to draw multi-color images on photonic crystal substrates using transparent imaging oils. Through the use of multi-oil inkjet printing we demonstrate the creation of custom images with the resolution down to 200 μm without the need for predefined template stamps[51]. The substrates can be returned to their initial state through the application of erasing oil and are compatible with low cost mass production techniques[52].

3.2 Experimental Section

The procedure for creating self-assembled colloidal photonic crystal (CPC) substrates can be found in earlier publications[51,53]. Here the CPC substrates are fabricated from monodisperse polystyrene (PS) nanospheres (Polysciences, Inc) 200 nm in diameter dispersed at 25mg/ml in pure water. Glass slides used to perform the assembly were first cleaned in 95% sulfuric acid for an hour to remove organic residues and make surfaces hydrophilic. Next the glass slides are rinsed with Acetone, 2-propanol (IPA), and DI water. To further increase the wettability, the glass slides are treated with oxygen plasma (Harrick Plasma) for one minute. To initiate the assembly process, 3ml of the PS dispersion solution was dispensed on the glass slides and then immediately covered with silicone oil (Gelest, Inc., Polydimethylsiloxane, DMS-T11, η = 10 centistokes (cSt) $\simeq$ 9.3497 centipoise (cP), Specific gravity (*SG*) = 0.935) to slow the evaporation process enabling long-range order to be obtained. Substrates were placed in an oven at 60 ℃ for several days while the assembly proceeded. After the water was completely evaporated, the silicon oil was carefully cleaned off. Premixed PDMS (1:1 mixture of PDMS base (Sylgard 184) and silicon oil (Gelest, Inc., Polydimethylsiloxane, DMS-T00, η = 0.65 cSt $\simeq$ 0.4946 cP, Specific gravity (*SG*) = 0.761) was then poured over the substrate allowing it to infiltrate into the interstitial spaces in the crystal.

3.3 Results and Discussion

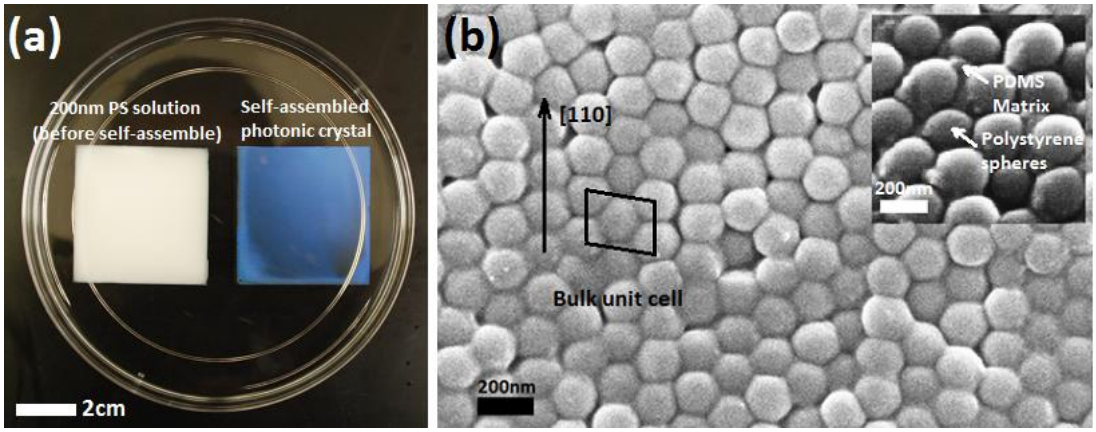

Figure 3 Self-assembled colloidal photonic crystal substrates. (a) Colloidal photonic crystal substrates were self-assembled on glass slides (5 × 5 cm) and are shown here in the initial amorphous state (left) and the crystalized state (right). After crystallization, the polystyrene spheres form a face-centered-cubic crystal structure which is fixed in a PDMS matrix. The substrate on the right exhibits a photonic bandgap at a wavelength of 489 nm. (b) SEM image of the self-assembled crystal structure showing a face-centered-cubic arrangement. The inset taken at a 30 ° tilted angle to better show the PDMS matrix being filled continuously in interstitial spaces among crystalized polystyrene spheres

Figure 3 shows a sample polystyrene colloidal photonic crystal (CPC) substrate used here, in both the amorphous state (left side) and the crystalline state following completion of the self-assembly based fabrication process (right side). The substrate fabrication technique exploits the capillary forces generated during solvent evaporation to drive the self-assembly[54] and we embed the final crystal structure in PDMS using a similar technique to that described by Fodouzi *et al.*[33,51] Details of the fabrication process are provided in the previous Experimental Section. As is shown in Figure 1 (b), the capillary force arranges the polystyrene (PS) beads in such a way that they form a face-centered-cubic crystal structure so that the [1 1 0] direction is parallel to the glass substrate. The number of layers in crystalline structure is determined by

the concentration of PS beads suspended in the solvent and the overall area of the substrate. In general, our structures comprised of about a hundred layers resulting in a substrate approximately 40 μm thick. Following formation of the crystal a liquid phase of premixed PDMS being polymerized later is infused into the voids via capillary action and solidified into the elastomeric form. Wohlleben *et al.*[55] also presented similar techniques to achieve elastic colloidal crystals exploiting a mechano-optical effect rather than the chemical-optical effect demonstrated here. Our CPC substrate is fabricated on fused silica for mechanical robustness that leads to potential applications such as fluidically-writable display demonstrated in this study. Thus in our investigation the elastic property of infused PDMS matrix is not the direct measure of reconfigurability as it was in that study[48].

For our CPCs the wavelength of the incoming light that will be most strongly reflected, λ_{ref}, can be approximated by the Bragg equation[53,56], $\lambda_{ref} = 2\ d_{latt}\ (n_{eff}^2 - \sin^2\theta)^{1/2}$ where d_{latt} is the lattice constant in the [1 1 1] direction, n_{eff} is the effective refractive index, and θ is the angle of the incidence[53,56]. From this equation, it can be seen that the wavelength of the light reflected from the CPC substrate is directly proportional to the lattice constant. It is noted that the wavelength of the reflected light also depends on the observation angle since it is function of the incident angle as in the Bragg equation above. Thus colors observed for our CPCs are seen differently from angle of view. Here we focus on the colors viewed at an angle of 90 degrees with the CPC substrate for the consistency. The dependency on viewing angle might limit some applications where colors must be consistent over broader viewing angles.

Locally swelling the lattice therefore will cause the reflected wavelength to increase. To accomplish this here, we use a series of different silicone oils as "colorless inks"[51]. When applied to the CPC substrate, silicone oils will diffuse into the polymerized PDMS matrix and cause it to swell[57] thereby increasing the interstitial distance and red-shifting the reflected wavelength (see Supplementary Movie S1). Silicon oils with larger molecular weights (*i.e.* different lengths of the $SiOC_2H_6$ monomer chain) cannot diffuse as readily into the PDMS matrix and thus tend to result in less steady state swelling than lower molecular weight variants and therefore a smaller red-shift.

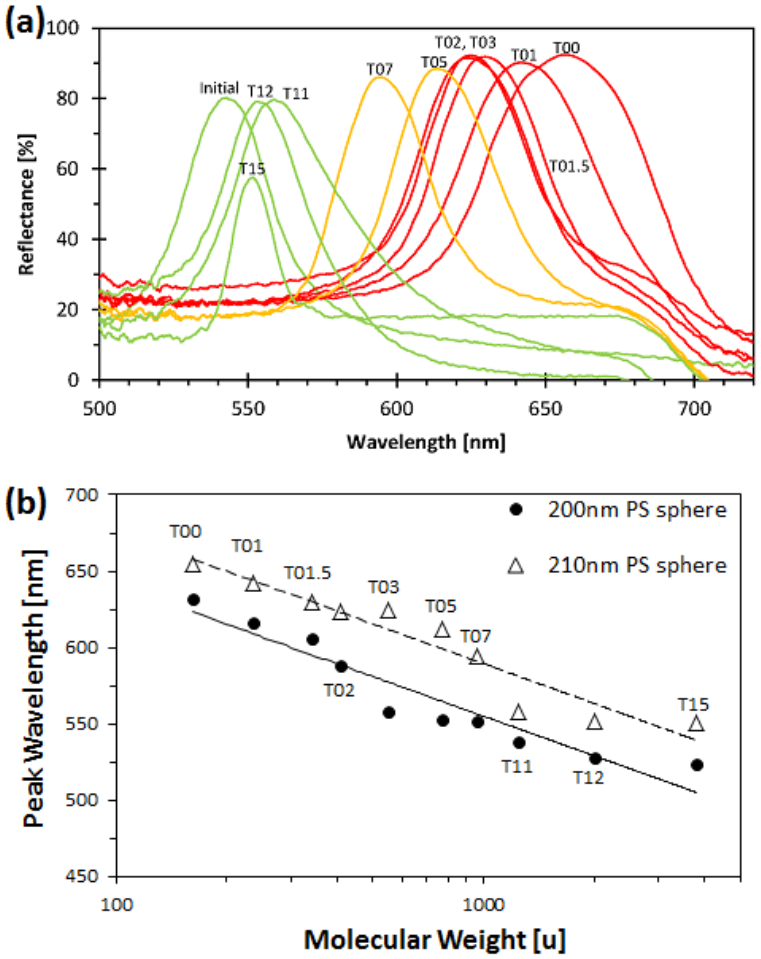

Figure 4 Color change in response to different imaging oils. (a) Reflected spectrum of a green photonic crystal substrate after application of different imaging oils. The index number of each silicone imaging oil is shown next to each curve. (b) Peak reflected wavelength as a function of the molecular weight of the imaging oils for both blue (200 nm beads) and green (210 nm beads) substrates.

Figure 4 shows the reflectance spectrum obtained from an initially green CPC substrate (peak reflectance 542nm) for the range of commercially available silicon oils (Gelest Inc., Morrisville, PA) from the high molecular weight T15 (molecular weight 3780 u) to the low molecular weight T00 (162 u). The peak reflectance wavelength for all the oils used here is plotted in Figure 2(b), using both initially blue (200 nm PS beads, represented with Δ) and green substrates (210 nm PS beads, represented with ●). As can be seen in both cases a linear response between the log of the oil's molecular weight and the reflected wavelength is obtained. This linear dependence of reflected wavelength is similar to that observed previously by Fodouzi *et al.*[51] In addition to being transparent and providing broad tunability, silicone oils have the additional advantages of being chemically non-toxic, having relatively low viscosity, and exhibiting low volatility.

To create high-resolution images on these substrates we make use of a Dimatix Material Printer which has the capability to deliver oils of different molecular weights and viscosities with high positional accuracy.

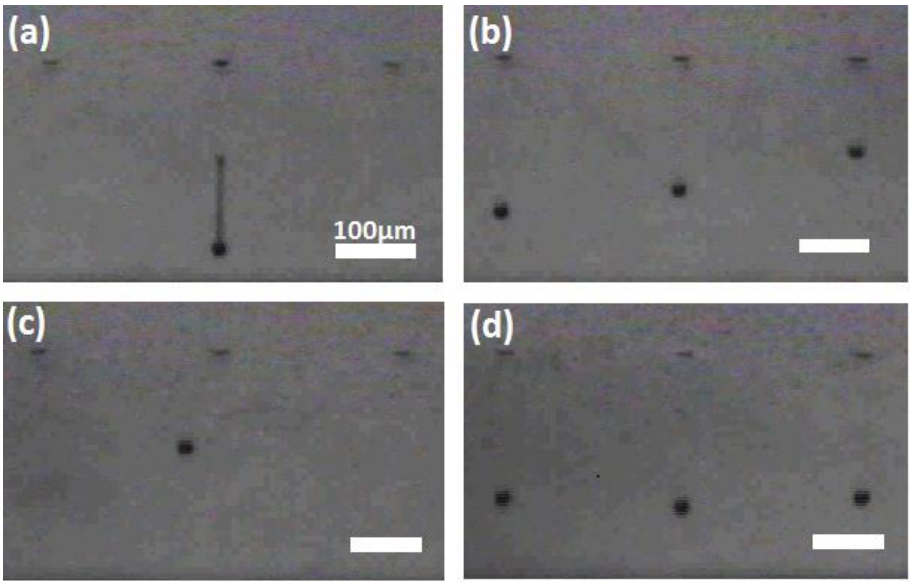

Figure 5 Droplet generation patterns using the Dimatix Material Printer. Representative cases of non-optimized droplets, such as (a) drops with ligaments (b) unsynchronized drops (c) stray drops, resulting in poor resolution. (d) Optimum three drops of 1pL volume. (Note that three holes on the upper side of the images are nozzles where droplets are jetted.)

As can be seen in Figure 5 by adjusting the driving voltage profile applied to the piezoelectric nozzle the size and shape of ejected droplet can be optimized. The achievable image resolution however is a function of both the droplet size and the diffusion distance within the substrate.

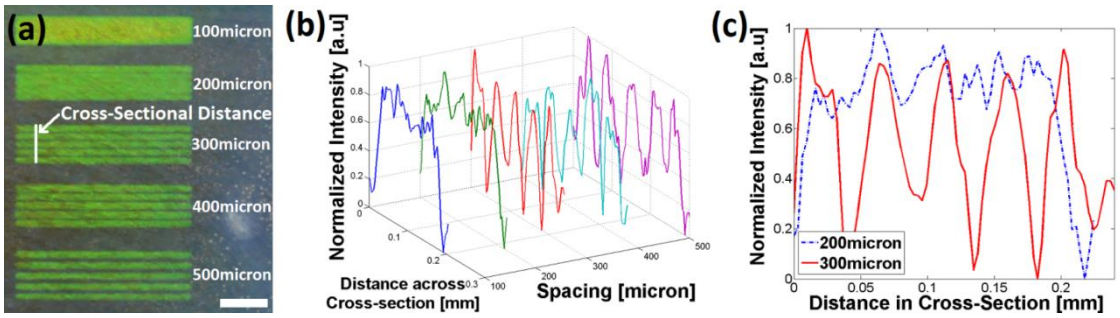

Figure 6 Characterization of the resolution limit of the imaging technique. (a) Test patterns transferred onto a CPC substrate consisting of five stripes (10mm length and 200 μm width), each with different spacing (100, 200, 300, 400, 500 μm) (b) Three dimensional plot of intensity profile normalized with the maximum intensity of each profile (c) Comparison between the 200 μm and 300 μm spacing profiles showing clearly resolved lines for the latter case and a blending of the lines for the former.

We estimate the resolution limit of the system using a series of test patterns consisting of stripes 200 μm wide, 1mm long, with spacing ranging from 100 μm to 500 μm as shown in Figure 6 (a). After transferring the test pattern to the CPC substrate, the intensity profile of across each pattern was analyzed using ImageJ and is plotted in Figure 6 (b). We define here the minimum achievable resolution as that above which the five discrete peaks could be clearly identified. Figure 6 (c) details the 200 μm and 300 μm spacing conditions where it can be seen that while the features blend together for the 200 μm case, with 300 μm spacing each separate feature is clearly distinguishable.

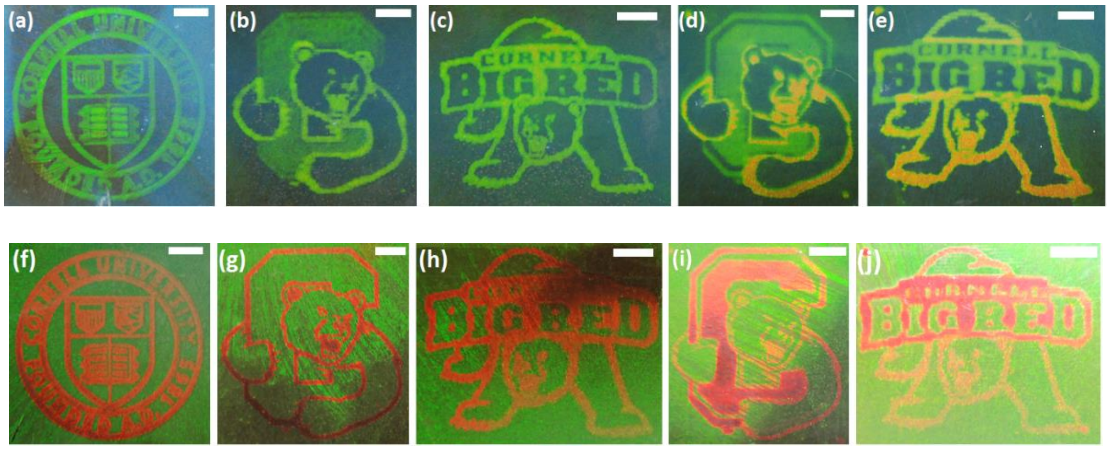

Figure 7 Demonstration of high resolution multi-color images printed on blue and green substrates (a)-(c) a series of images represented with a single printed color, green (T11), on a blue CPC substrate (d), (e) Multicolor green and orange images printed using T11 and T03 oil respectively. (f)-(h) the same images shown in (a)-(c) printed in red (T03) on a green CPC substrate (i), (j) multi-color red (T03) and orange (T11) images on a green substrate. All scale bars in the images are 1 mm.

Three different images of varying complexity and color range are recreated in Figure 7. The first three images in Figure 7 show the logos of Cornell University (a, which contains fine features and letters), and Cornell Athletics (b,c) transferred to the blue CPC substrate with a monochrome green ink. Figure 7 (f, g and h) show similar images transferred to the green CPC substrate in a monochrome orange ink. The remaining images show three color image replications where the logos are separated into two different sections, with parts colored using the T03 and T11 oils respectively. On the blue CPC substrate, this results in blue, green (T11) and orange (T03) images, and on the green CPC substrate this results in green, orange (T11) and red (T03) images. Although for low resolution images, the color change was instantaneous, for the high resolution images, between 5 and 7 minutes were required for the full image to form. This includes the time for pattern transfer and for the relatively small amount

of oil to fully diffuse into the base substrate. In uncontrolled environments, the image stability is governed by the evaporation rate of the oils which in itself is dependent on the molecular weight. The oils with relatively large molecular weights created images that tended to last for several days or weeks (T15 (over a month), T05, T07, T11 and T12 (10-15 days), T02 and T03 (4-5 days)), whereas the oils with smaller molecular weights could evaporate in as little as a few minutes (T01 and T01.5 (2-3 minutes)).

The low vapor pressure of the low molecular weight oils can be exploited to erase transferred images and the reset the substrates. The lowest molecular weight T00 silicone oil exhibited a very low viscosity enabling it to penetrate deep into the photonic crystal structure and mix with and dilute any existing image producing oils, then promptly evaporate within a few seconds.

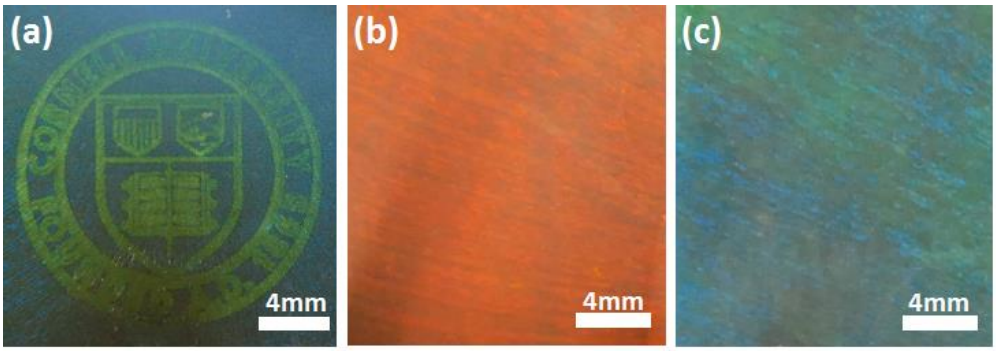

Figure 8 Rapid erasing and reuse of printed images. Sequence of the images demonstrating reusability of the substrates by erasing patterns with the silicone oil (DMS T-00). (a) The image was transferred to the CPC substrate. (b) A few seconds after applying the erasing oil, the substrate turns red as the oil diffuses into the crystal. (c) After evaporation, the substrate of the colloidal photonic crystals turns back into initial color without a trace of the previous image.

Figure 8 shows sequential images of (a) an image displayed on the CPC substrate (b) the same substrate following application of the T00 oil and (c) the original image location after evaporation of the T00 erasing oil (see Supplemental Movie S2). As can be seen the substrate is returned to the original color without a trace of the original image. The erasing procedure takes less than 10 seconds after the T00 oil is applied. We have been able to use this procedure in excess of 30 times without the degeneration of the original substrate or reduction in the quality of the reproduced images. The CPC substrate can be reused in the writing and erasing cycle without degradation unless the photonic crystal structure in PDMS matrix is physically damaged (for example) by scratching. For a potential application as writable display additional PDMS layer on top of the CPC substrate could provide greater robustness. This could however increase the diffusion time for the oils and slightly degrade the image quality due to the additional diffusion distance.

3.4 Conclusions

In this paper, we have demonstrated the use of self-assembled colloidal photonic crystal substrates to support high resolution, multi-color, stable but erasable images printed with transparent silicon oils of varying molecular weight. We expect that such a technique could find applications in the development of new flexible and stretchable drawing substrates and low power reflective display technologies.

Chapter 4

ANGULAR ORIENTATION OF NANORODS USING NANOPHOTONIC TWEEZERS

4.1 Abstract

Near-field optical techniques have enabled trapping, transport, and handling of nanoscopic materials much smaller than what can be manipulated with traditional optical tweezers. Here we extend the scope of what is possible by demonstrating angular orientation and rotational control of both biological and non-biological nanoscale rods using photonic crystal nanotweezers. In our experiments, single microtubules (diameter 25 nm, length 8 μm) and multi-walled carbon nanotubes (outer diameter 110 – 170 nm, length 5 μm) are rotated by the optical torque resulting from their interaction with the evanescent field emanating from these devices. An angular trap stiffness of κ = 92.8 pN nm/rad^2-mW is demonstrated for the microtubules and a torsional spring constant of 22.8 pN nm/rad^2-mW is measured for the nanotubes. We expect that this new capability will facilitate the development of high precision nanoassembly schemes and biophysical studies of bending strains of biomolecules.

4.2 Introduction

In 1987, Ashkin *et al.*[20,21] showed that a single rod-shaped cell and bacteria and viruses could be trapped and oriented with laser beams, demonstrating optically induced rotation along with the optical trap[1]. In biophysical studies the orientation control of elongated objects is significant because numerous biomolecules such as DNA, viruses, and bacteria can take rod-like shapes[58]. Optical torque arises from the

exchange of angular momentum between an electromagnetic field and a physical object. Circularly polarized laser beams carry angular momentum which can lead to a torque on dielectric objects[59-61]. Another general method is to take advantage of the interaction of anisotropic dielectric objects with light fields to provoke the change in angular momentum[62]. Padgett and Bowman[63,64] recently reviewed the various methods for applying optical torques with conventional optical tweezers.

This capability is well established for traditional optical tweezers[63-66], but has not been addressed in the near-field trapping literature. Near-field optical traps are of particular interest because they allow for the trapping of smaller materials than conventional optical tweezers[28]. These devices take advantage of the increased gradient force exerted on particles due to a combination of highly confining light geometries and increased intensity due to resonances. Several different device structures have been exploited to this end including photonic crystal resonators[26,67], ring resonators[68], and localized surface plasmons[69,70] each providing very deep trapping potentials. Researchers have investigated ways of taking advantage of the interaction of different polarizations of light with specially designed plasmonic structures to tune the position of trapped spherical particles around a plasmonic cylinder[70] or to continuously rotate a plasmonic object[71]. To date however the ability to simultaneously optically trap and reorient an unstructured nanoscale object has not been demonstrated. Orientation control is a particularly important issue to address for trapping of nanoscale objects since as the size of the trapped object decreases the rotational diffusion coefficient increases (analogous to linear diffusion). Adding

orientation control to the capabilities listed above would allow for tight control over five out of six degrees of freedom

4.3 Experimental Section

In this paper, we characterize the optical torque arising in one dimensional photonic crystal resonators and demonstrate the orientation of rod-like biological (microtubules, MTs) and non-biological (carbon nanotubes, CNTs) materials. First, the dynamics of the orientation of MTs in the cavity of a photonic crystal resonator will be examined at different trapping laser powers and compared with an analytical model. In the second section we examine the capacity of the optical trap to maintain a rod's orientation and described it in terms of a torsion spring model. Experimental measurements of the torsion spring constant have been performed for the two materials of interest here (MTs and CNTs) to demonstrate the broad applicability of the technique. Finally, dynamic control over the orientation of carbon nanotubes via hydrodynamic flow is also demonstrated. Experiments with biological samples are performed with a silicon nitride photonic crystal resonator operating at 1064 nm in a biological buffer (which was previously verified not to undergo significant temperature increase[67]), whereas the experiments with carbon nanotubes were performed with silicon resonators in heavy water operating at 1550 nm. Figure 9 displays a schematic view of the photonic crystal with a microtubule. Microtubules of $L \sim 10$ μm and $D \sim 25$ nm were used in all the microtubule experiments. Multiwall carbon nanotubes of outer diameter 110-170 nm were used in this work. Details of the

experimental procedures and device fabrication techniques are provided in the methods and materials section of the Appendices B .

4.4 Results and Discussions

4.4.1 Orientation Dynamics

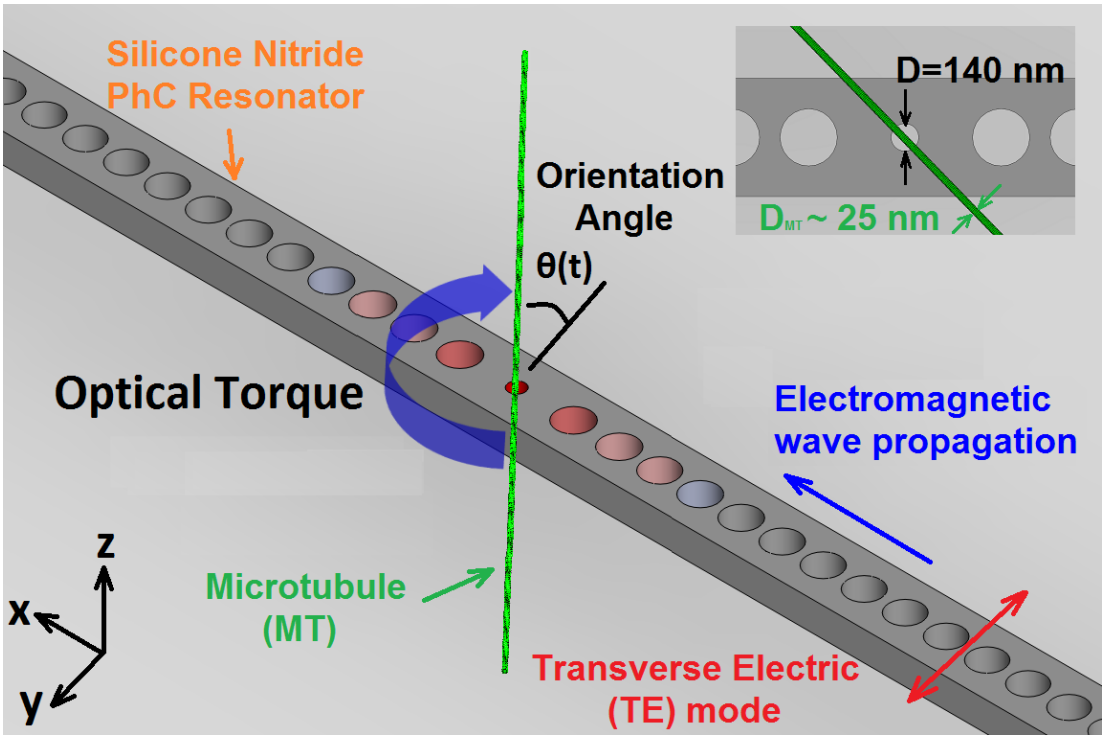

Figure 9 Schematic of the orientation of a microtubule on a photonic crystal resonator. The electromagnetic wave propagates in the x direction (blue arrow), with a polarization of transverse electric field (TE) along the y axis (red arrow). A microtubule comes close to a resonator with an orientation angle, θ, and is oriented parallel to the polarization direction. The field of a TE mode gives rise to an optical torque (blue curved arrow) that acts on the microtubule. The orientation angle at time *t*, θ(t), is measured with the respect to the y axis. (Inset: the diameter of the center cavity in resonator is D = 140 nm whereas the diameter of a microtubule is D ~ 25 nm)

The orientation process of a dielectric object in the presence of an electric field is described by dipole moment theory[58,72]. The microtubules in this study are modeled as dielectric ellipsoids[73]. When a dielectric ellipsoid is placed in an electric field such that the long axis of the ellipsoid is at an angle θ to the direction of the electric field as defined in Figure 1, a torque is generated with magnitude $\boldsymbol{T_o}$ = ½ Re[$\boldsymbol{p} \times \boldsymbol{E}^*$], where the vectors quantities are in bold letters, the vectors $\boldsymbol{p}$ and $\boldsymbol{E}$ are complex valued polarizations and external electric field, * denotes a complex conjugate and Re[ ] denotes the real part. The electric field induces a dipole moment expressed as $\boldsymbol{p} = \overline{\overline{\boldsymbol{\alpha}}} \cdot \boldsymbol{E}$, where $\overline{\overline{\boldsymbol{\alpha}}}$ is the polarizability tensor. The induced torque is expressed by T = ½ α_{eff} $E^2 \cos\theta \sin\theta$, where E = $|\boldsymbol{E}|$, α_{eff} = Re[$\overline{\overline{\boldsymbol{\alpha}}}_{long} - \overline{\overline{\boldsymbol{\alpha}}}_{trans}$], $\overline{\overline{\boldsymbol{\alpha}}}_{long}$ and $\overline{\overline{\boldsymbol{\alpha}}}_{trans}$ are the polarizabilities of the ellipsoid along the longitudinal axis and the transverse axis respectively.

As the microtubule starts to rotate under the action of the electromagnetic field, it experiences a hydrodynamic countertorque $T_{\text{h}} = \pi l^3 \mu C_{\text{r}} \dot{\theta}$, where μ is the viscosity of the medium, C_{r} is the rotational hydrodynamic drag coefficient expressed as $C_{\text{r}} = [3(\ln(l/r) - ½)]^{-1}$, and $\dot{\theta}$ is the first derivative of the angle with respect to time[73]. This countertorque is equivalent to hydrodynamic drag for linear motion. The balance between the induced torque and the hydrodynamic countertorque leads to the equation of motion for the orientation process (5) and its analytic solution (6):

$$\tau\dot{\theta} = -\cos(\theta)\sin(\theta) \tag{5}$$

$$\ln(\tan(\theta)) = \ln(\tan(\theta_0)) - \frac{t}{\tau} \tag{6}$$

In the previous equations the symbol τ is the time constant of the orientation which is expressed as $\tau = 2\pi l^3 \mu C_r/(\alpha E^2)$.

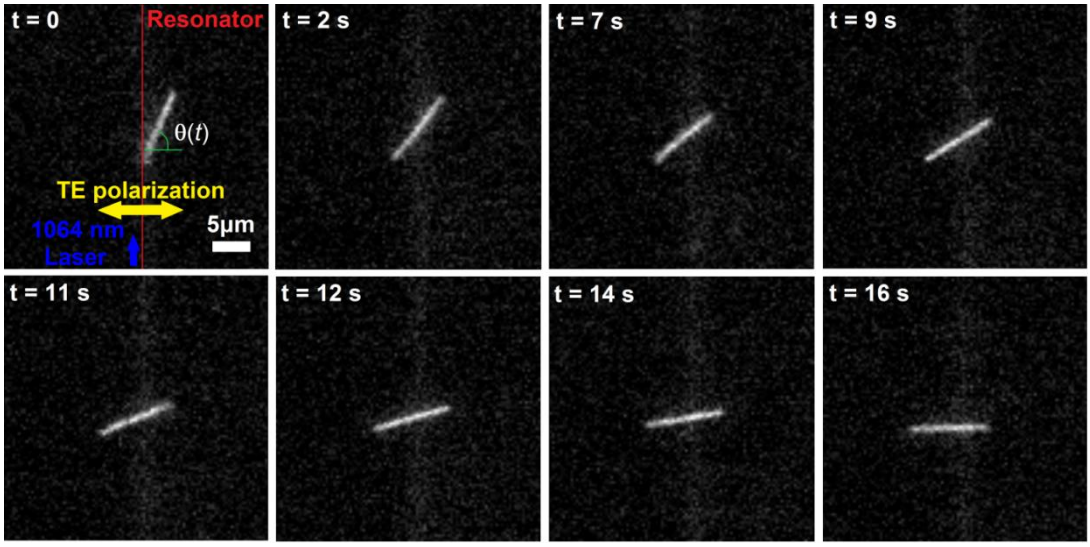

Figure 10 Sequential images of the orientation of a microtubule observed by epifluorescent microscopy using the fluorescent-labeled microtubule (bright line). The orientation was observed until the microtubule is parallel to the direction of the electric field (yellow arrow in t = 0). The length of the microtubule is estimated to be 10 μm and the diameter is 25 nm. The silicon nitride photonic crystal resonator is centered and vertical (red line in t = 0). The electromagnetic field propagates through the resonator from bottom to top. The frames are extracted from full movie available in supplementary movie 1.

Figure 10 illustrates how a single microtubule is oriented by the optical torque in the evanescent field of a silicon nitride photonic crystal resonator. The microtubule is initially oriented at 70 degrees to the field polarization. It is then moved as close as possible to the resonator using a slow flow rate (u = 1 μL/hr) from left to right. When it moves onto the resonator and starts to interact with the electric field, it is polarized by the electric field and experiences the optical torque. As a result it is aligned with

the field. The time constant of the orientation, τ, was determined by measuring the orientation angle as a function of time.

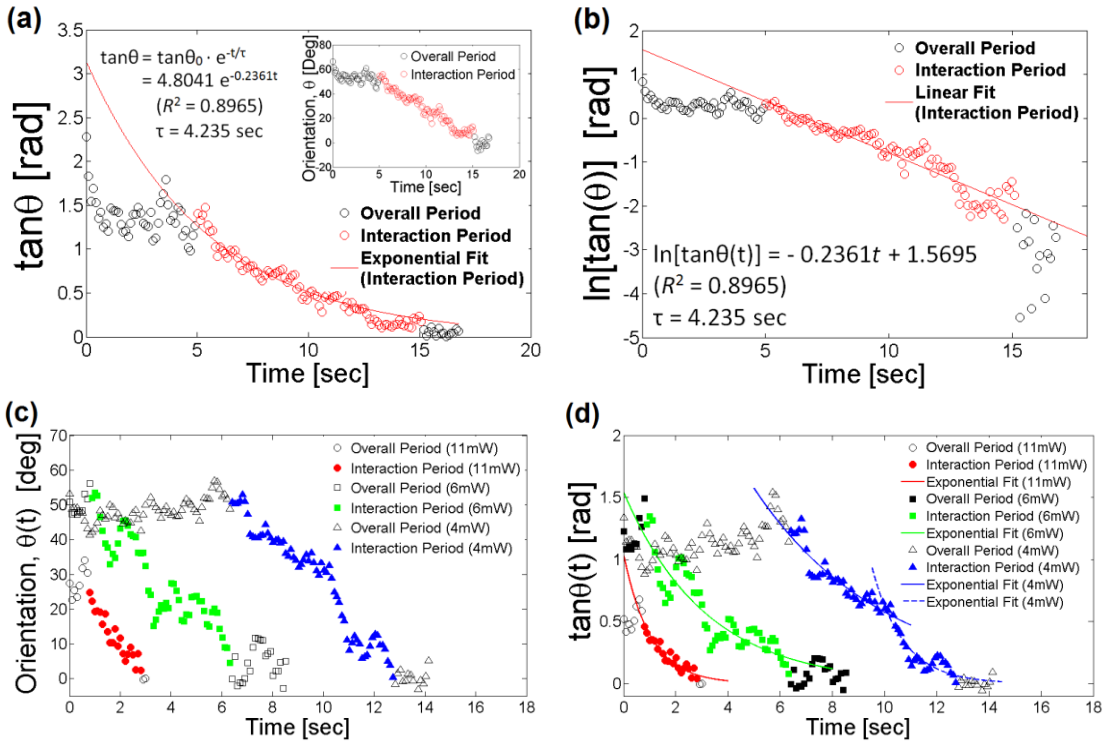

Figure 11 Quantitative analysis of the orientation of the microtubule interacting with the cavity of a photonic crystal resonator. (a) Inset: experimental measurement of the orientation angle in degrees versus time while the microtubule is being oriented by the electromagnetic field. Main Figure: exponential fit of tan(θ(t)) from these measurements. The time constant is τ = 4.235 sec as determined from the fitting. The red dots correspond to the time period when the microtubule is interacting with the resonator, as evidenced by the good agreement between the analytical model and the experimental curve. (b) The time constant was also determined by a linear regression to $\ln(\tan\theta) = \ln(\tan\theta_0) - t/\tau$. In the interaction period (red dots), the analytical model and the experimental curve are in good agreement ($R^2 = 0.8965$). (c) Orientation of microtubules with varying optical power (4 mW (Δ), 6 mW (□), 11mW (○)) coupled into the resonator. The period of interaction with the resonator was highlighted with color-filled markers (4 mW (▲), 6 mW (■), 11mW (●)). (d) The time constants were determined by exponential fitting of the interaction period of tan(θ(t)) (τ = 4.975 sec (4mW), τ = 3.125 sec (6mW), τ = 1.041 sec (11mW)). In the highlighted interaction period, the analytical model and the experimental curve are in good agreement ($R^2 = 0.86$ (4mW), $R^2 = 0.7699$ (6mW), $R^2 = 0.8155$ (11mW)). The time constant was τ = 1.203 sec ($R^2 = 0.6111$) after the transition (— → ---) as described in the main text.

Figure 11 (a) and (b) show the measured orientation angle with respect to time for the data set shown in Figure 10 (the estimated power coupled into the resonator is 16 mW). The quantitative orientation measurements were performed in ImageJ[66] with the plugin OrientationJ[74]. The plot of $\ln(\tan\theta(t))$ was verified to be linear with respect to time ($R^2 = 0.89$). The slope of the linear fit of $\ln(\tan\theta(t))$ is $1/\tau$ where τ was determined to be 4.235 s from these experiments. The good linear fit indicates that the orientation of the microtubule in this experiment is not the result of random thermal fluctuations but the effect of the electric field acting on it. In Figure 11, the highlighted markers correspond to the portion of the curves where the microtubule interacts with the field. The beginning of the interaction period was considered the time when the orientation angle begins to decrease continuously. The time can be quantitatively determined by finding a cross point where the fitting of constant orientation angles and that of exponentially decaying $\tan\theta$ curves cross each other. Deviations of the measured curve to the fitted approximation is attributed to errors in the angle measurement, and to fluctuations in the electric field acting on the MT as it moves along the resonator and as its height fluctuates.

Figure 11 (c) and (d) display the orientation process for different input power. The time constants were determined to $\tau = 4.975$ s (4mW), $\tau = 3.125$ s (6mW), $\tau = 1.041$ s (11mW). Because small variations in the initial position of the microtubule in the experiment led to large changes in the electric field it experiences, a quantitative verification of the relation could not be performed. In addition to the varying electric field along photonic crystal cavities, varying polarizability of a microtubule makes it difficult to determine experimentally the time constant, $\tau = 2\pi l^3 \mu C_r/(\alpha E^2)$,

We compare these time constants to those reported by Minoura and Muto[73] who showed $\tau = 0.4$ s for a microtubule of the same length. They used an electro-orientation system that applies an alternating electric field ($0.5\text{-}1.9\times10^5$ V/m, 10 kHz - 3 MHz) to orient the microtubule but doesn't trap them. The orientation times in this study is longer. This might be the result of: the dielectric response of the microtubule at 1064 nm (280 THz) compared to that at lower frequencies, viscous coupling with the substrate, and the shorter interaction region between the field and the microtubule in this setup. For the lowest coupled power, 4 mW, the exponential fit was observed to break down in the middle. Two distinct interaction periods are noticeable, the earliest is labeled with a continuous line (—) and the latest with dotted line (---). The transition (— → ---) was observed during the interaction period and might be the result of the microtubule being pushed from one optical hotspot to another. The time constant in the earlier region was $\tau = 4.975$ s (—) whereas it was $\tau = 1.203$ sec ($R^2 = 0.6111$) after the transition (---) signifying that the interaction with the later hotspot was stronger. Figure 18-b (ii) illustrates the stronger hotspot along the photonic crystal cavities.

4.4.2 Torsion Spring Model and of Angular Trap Stiffness

The previous expression of the electromagnetic torque can be simplified for small angles where the torque can be seen to vary linearly with the angular displacement described by a torsional spring model on the nanorods[65]. This enables us to determine the strength of the torsional trap in direct analogue to the way spring stiffness models are used to characterize the stability of a positional trap. To verify

the torsion spring model is valid for dielectric rods smaller than the electromagnetic hotspot, we first developed a Finite Element Method (FEM) model of a nanorod-resonator system using COMSOL. In the model the probe object is a 2 μm long, 40 nm diameter, anisotropic rod (the axial permittivity was set to 12 and the transverse permittivity is that of water). The torque was calculated from the Maxwell stress tensor as a function of the orientation of the rod. The following quantity was integrated over a surface enclosing the rod:

$$\boldsymbol{T} = \oiint \boldsymbol{r} \times \overline{\overline{T}}_{Maxwell} \cdot \boldsymbol{n}\, dS \tag{7}$$

Where $\boldsymbol{r}$ is the position vector with respect to the center of the rod, $\overline{\overline{T}}_{Maxwell}$ is the Maxwell stress tensor, $\boldsymbol{n}$ is the outgoing normal to the integration surface. The result of the integration of the torque tensor was found to take a sinusoidal shape with angular period π consistently with Equation (5) where $\sin\theta\cos\theta = 1/2\sin 2\theta$.

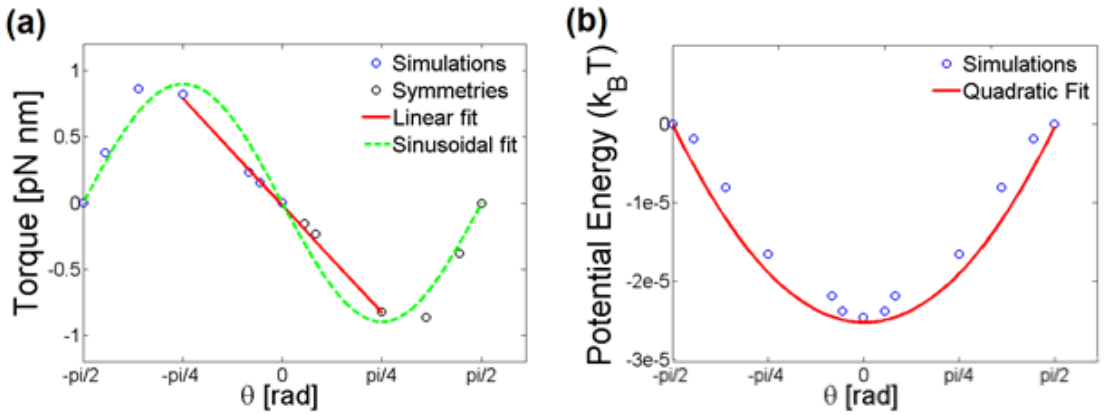

Figure 12 (a) Numerical computation of the torque exerted on an anisotropic rod by the means of Equation (3). The model rod is a 2 μm long, 40 nm diameter, anisotropic rod with longitudinal permittivity 12 and axial permittivity 1.72 same as the background water; it was placed 50 nm above a photonic crystal resonator on resonance[75] for angles in [-π/2,0]. Red dots represent the numerically estimated torques, blue dots represent the extrapolated ones with symmetries, the green dotted line is a sinusoidal fit. The red line is a linear fit around θ=0 where the torque is linear in θ. (b) Rotational potential energy evaluated by integrating the torque with respect to θ. Red solid line is the quadratic potential to the linear fit in (a). Assuming a sinusoidal fit of the form sin(2θ) as displayed in (a), the quadratic potential should be valid for small angles where sin(2θ) is close to its first order Taylor expansion: 2θ.

The plot of this torque is presented in Figure 12(a). Around the stable trapping position ($\theta = 0$ in Figure 1) the torque can be seen to vary linearly with respect to θ as one would expect considering the Taylor expansion of the sinusoidal fit. The plot of this torque is presented in Figure 12(a). Around the stable trapping position ($\theta = 0$ in Figure 1) the torque can be seen to vary linearly with respect to θ. A torsion spring representation of the torque in this region was therefore chosen to characterize the trapping properties of the photonic crystal resonators on the rods. Torsion springs are characterized by a constant κ called torsion spring constant. The torque and potential energy are given by:

$$\boldsymbol{T} = -\kappa\boldsymbol{\theta} \tag{8}$$

$$U_P = \frac{1}{2}\kappa\theta^2 \tag{9}$$

In these equations $\boldsymbol{T}$ is the torque and U_P is the potential energy. The potential energy was calculated from the torque and is presented in figure 12(b).

This way to describe the trapping capacity of photonic crystal resonator is useful as energy potentials allow for an easier comparison to other forces at play[76]. The torsion spring constant is linked to the angular spread measured experimentally through the equipartition theorem which, in the torsion spring model, reads:

$$\frac{1}{2}k_B T = \frac{1}{2}\kappa\left\langle\theta^2\right\rangle \tag{10}$$

In this equation k_B is the Boltzmann constant and T is the temperature in Kelvin.

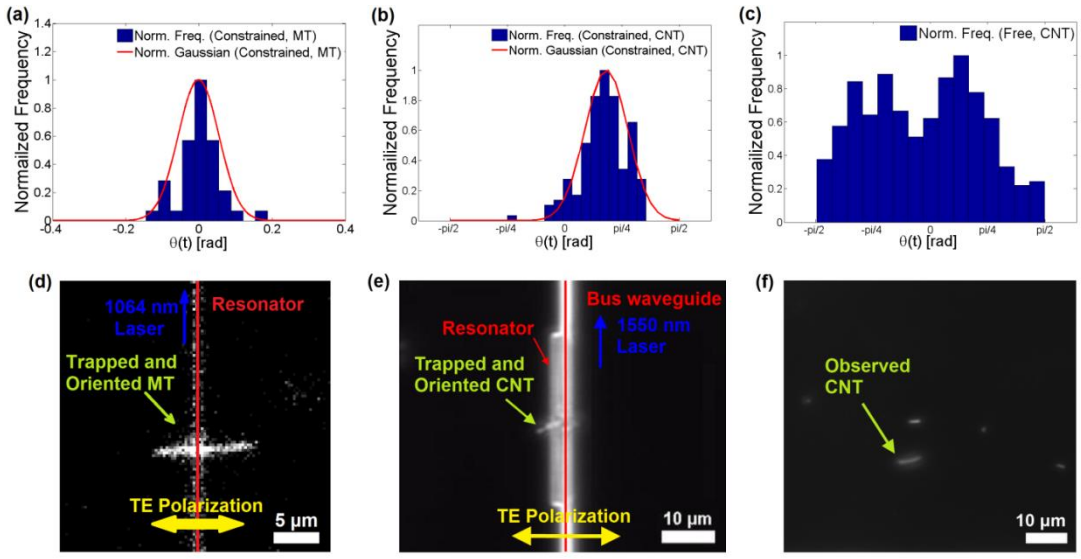

Figure 13 Analysis of the angular orientation of a trapped microtubule, carbon nanotube and a freely diffusing carbon nanotube. The angles were acquired every 0.1 second. (a) Histogram of orientations of a trapped microtubule. The red solid line represents a Gaussian fit. (b) Histogram of orientations of a trapped carbon nanotube. The red solid line represents a Gaussian fit. (c) Histogram of orientations of a freely diffusing carbon nanotube taken at the same focal plane as the resonator to account for viscous coupling with the Debye layer at the surface of the microchannel. (d-f) Sample frames from the data sets displayed in frames (a-c) respectively.

For microtubules, the torsional trapping stiffness was determined from Figure 13 (a) to be κ = 92.8 pN nm/rad^2-mW (the torsion spring constant was normalized to the estimated power in the cavity). The probability density of the orientation angles established by the Boltzmann statistics is expected to be a Gaussian function. The width of the Gaussian-shaped histogram equal to the time-averaged squared angular displacement, $\langle\theta^2\rangle$, is related with the angular trap stiffness κ by Equation (10). The average angular orientation θ_{mean} was measured from the center of the distribution was measured to 5.1 ° (0.088 rad) and the standard deviation was determined to σ = 3.1 ° (0.055 rad). Microtubules are representative of a dielectric material where the torque

exerted by the photonic crystal should be well modeled by our spring constant analogy as illustrated by our numerical simulations. Because of the possible surface plasmon resonances in carbon nanotubes, they represent a special case of the theory. If the wavelength and k-vector coincide with a resonance of the CNT, the electric field will be further amplified as well as the torque. We account for this by making the trapping stiffness a function of θ: $\kappa(\theta)$. In the simplest approximation, $\kappa(\theta)$ is a Lorentzian bell with a peak at $\theta = \theta_{mean}$. In this approximation the trapping stiffness at the steady position can be found through the equipartition theorem with $\kappa = \kappa(\theta_{mean})$. We present in Figure 13 (b) and (c) the comparison of the distribution of angles in the case of a trapped CNT and a freely rotating one (near the bottom of the microchannel). From Figure 13 (b) we compute the central stiffness to κ = 22.8 pN nm/rad^2-mW in the same manner as described for a microtubule (normalized to the estimated power in the cavity).

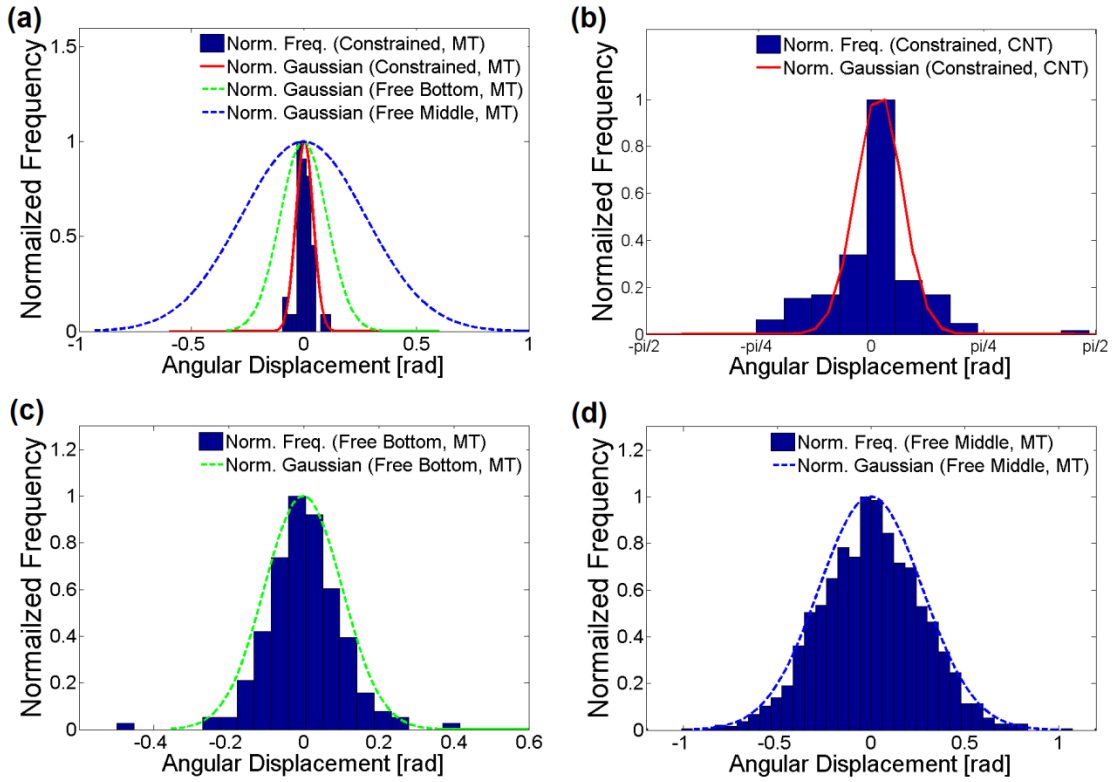

Figure 14 Histograms of angular displacement of trapped nanorods and of their free rotational Brownian motion. The orientation angle of the microtubule as a function of time $\theta(t)$ is measured every 0.1 second. The angular displacement as a function of time $\Delta\theta(t) = \theta(t + \tau_0) - \theta(\tau_0)$ is calculated for all angular trajectories with starting times, τ_0. (a) Comparison of the Probability Density Functions (PDF) of $\Delta\theta(t)$ for t = 0.1 s for a trapped microtubule and free ones. The normalized histogram (blue bars) and the normalized Gaussian fit (red solid line) of the constrained rotational Brownian motion are shown along with the normalized Gaussian fits of free rotational Brownian motion. (b) PDF of the angular displacement for t = 1 s of a trapped carbon nanotube. (c) PDF histogram (blue) and Gausian fit (green dotted line) of the angular displacement of a freely rotating microtubule at the same focal plane as the resonator to account for viscous coupling. (d) PDF histogram (blue) and Gausian fit (green dotted line) of the angular displacement of a freely rotating microtubule at mid-channel height.

As can be seen from Figure 14 (b), the most likely position for the CNT was not orthogonal to the resonator (position labeled 0 in Figure 10), but at an angle of 35 degrees (0.61 rad). This is attributed to hydrodynamic forces, the shape of the CNT. Tong *et. al*[77] recently shown that plasmonic nanowires can orient orthogonally to the light polarization in optical tweezers if the beam waist is smaller than their length. Because of the difficulty in numerically modeling CNTs, the experimental results of this work were not compared to theoretical predictions. The torsion stiffnesses in this study can be compared to that exerted by a far field optical tweezer. Porta and Wang[65] demonstrated an optical torsion in the order of several 100s pN·nm for angular velocities up to 200 rad/s using an optical power of ~ 10 mW on ~1 μm diameter quartz particles as compared to our 25 nm diameter microtubules.

The rotational motion was reduced when the nanorods were optically trapped and oriented, as shown in the previous paragraph. Additionally, the rate of diffusion was also found to be affected by the optical torsion spring. For a quantitative study of this observation, the rotational diffusion coefficient for MTs and CNTs in the presence and absence of the optical field were calculated from the measured angular displacements. The rotational diffusion coefficient relates to the angular displacement through the relation $D_\theta = \langle[\Delta\theta(t)]^2\rangle/(2t)$, where $\langle[\Delta\theta(t)]^2\rangle$ is time-averaged squared angular displacement[78]. The rotational Brownian motion of a freely rotating microtubule was observed at different heights in the flow channel. The rotational diffusion coefficient at the bottom of the channel ($D_{\theta,\,\text{free, MT}}' = 5.366\times10^{-2}$ rad^2/s) was lower than at mid channel height ($D_{\theta,\,\text{free, MT}} = 3.825\times10^{-1}$ rad^2/s) owing to viscous coupling[73] (Figure 6 (c) and (d)). The penetration depth of the evanescent field is a

couple hundreds of nanometers from the PhC resonator. The rotational diffusion coefficient at the bottom of the channel was measured for a microtubule that was in the same focal plane as the one influenced by the PhC resonator. The rotational diffusion coefficient is inversely proportional to viscosity as $D_r = k_B T/\pi\mu l^3 C r$, where C_r is a form factor $C_r = [3(\ln(l/r) - 1/2)]^{-1}$. The hydrodynamics coupling resulting from 7 times larger viscosity resulted in lesser rotational diffusivity at the bottom of the channel. The reduction of the rotational diffusion by 7.13 times is consistent with the consideration of larger viscosity by a factor of 7. The apparent diffusion coefficient of an optically oriented microtubule, also at the bottom of the channel, was further reduced to $D_{\theta,\,\text{cons, MT}} = 1.473\times10^{-2}$ rad^2/s, lower by a factor of 3.7 from $D_{\theta,\,\text{free, MT}}$ as seen in Figure 14 (a). Similarly, the diffusion coefficient of a carbon nanotube measured at the bottom surface ($D_{\theta,\,\text{free, CNT}} = 7.2\times10^{-2}$ rad^2/s) was observed to be higher by a factor of 3.1 than for a trapped CNT where we found $D_{\theta,\,\text{cons, CNT}} = 2.3\times10^{-2}$ rad^2/s (Figure 14 (b)).

4.4.3 Hydrodynamic Torque

The previous experiments were performed with little to no fluid flow in the microfluidic channel. Fluid flows, however, can balance the optical torque and offer another way to dynamically control the orientation of trapped nanorods. We describe here in qualitative terms the influence of the hydrodynamic torque on their orientation.

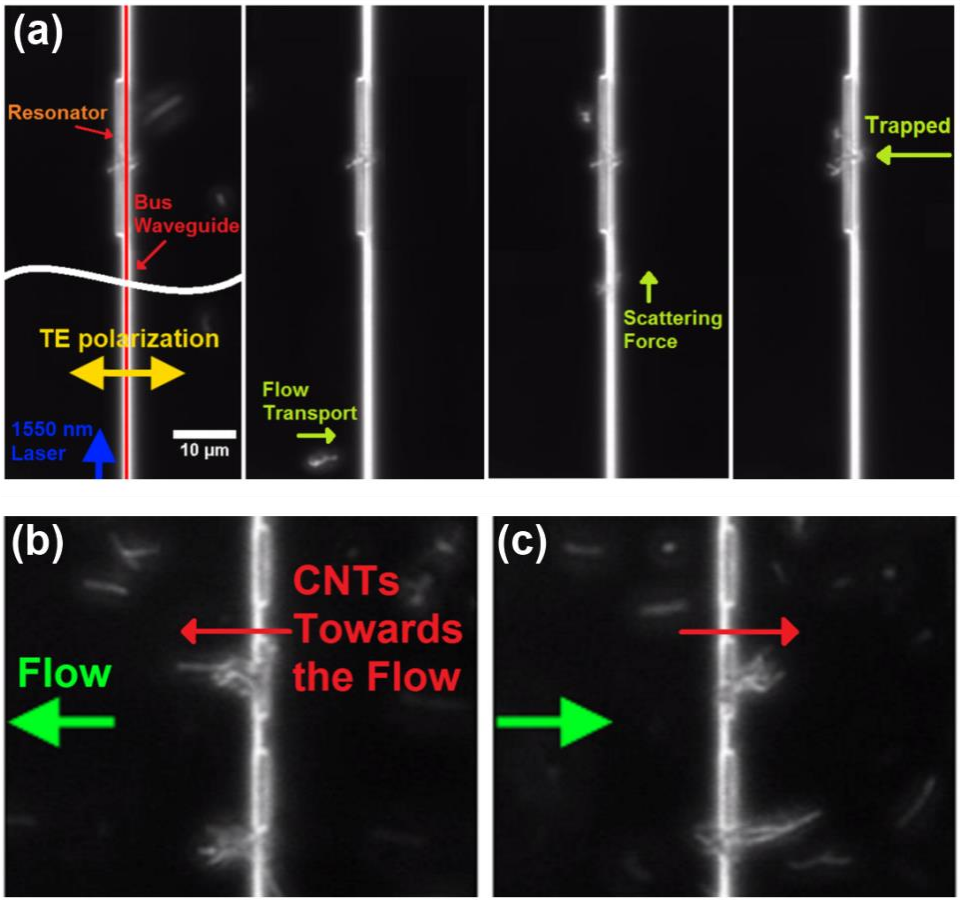

Figure 15 (a) Sequential image of trapping and orientation of a carbon nanotube observed under dark field microscopy. In the first image, a carbon nanotube is already trapped on the silicon PC resonator, another one is transported along the bus waveguide to the resonator where it remains trapped. Time lapse between the first and last frame is 10 s. For the sake of clarity, the images were retouched removing non-essential components (b) and (c) Time lapse images of carbon nanotube aggregates. By switching the direction of the flow (green arrow), the hydrodynamic forces align the carbon nanotubes with the flow while the optical trap pins them to the resonator. (b) A flow rate of 30 µL/hour is applied with a mechanical syringe pump right to left. The carbon nanotubes point in the direction of the flow. (c) The flow direction is reversed, the nanotubes reorient to point in the direction of the flow. In this experiment, the flow channel was orthogonal to the bus waveguide.

In these experiments, hydrodynamic forces affect the CNTs initially as they are propelled upwards by the radiation pressure along the resonator as seen in Figure 15 (a). This radiation pressure transport along waveguides affect has been documented previously in our other works[26]. When moving along the resonator, the hydrodynamic forces tend to orient the nanotubes along their direction of motion (90 degrees in our convention from Figure 10) until they come to the trap where they are quickly reoriented back to the orthogonal position. The hydrodynamic resistance becomes minimal as nanotubes orient along the moving direction. The motion of a carbon nanotube transported along the waveguide to the resonator where it remains trapped is noted in experiment. It is also observed that the resonator can only support two carbon nanotubes at a time. A third nanotube does not get trapped and is pushed upwards along the waveguide similarly to what was described by Cai *et al.*[79] in their tapered waveguide.

Hydrodynamic forces can also be used to actively orient the trapped carbon nanotubes. The carbon nanotubes were observed to be preferentially trapped close to their extremities. Taking advantage of the flow, which was orthogonal to the resonator, the carbon nanotubes were oriented left or right as shown in Figure 15 (b). The flow was applied with a mechanical syringe pump set at 30 μL/hour. At the surface of the substrate, the flow speed is lower because of the parabolic flow profile in a microchannel. The flow speed was estimated assuming the smallest carbon nanotubes are good flow tracers. With this method the flow speed at the surface was measured to be 7.12 ± 1 μm/s. With more microfluidic ports, the orientation of the trapped

nanotubes could have been chosen to cover nearly 2π spread with the microfluidic assembly line proposed by Schneider *et al.*[80].

4.5 Conclusion

Along with the ability to confine nanoscale material in solution, constraining their orientation ensures a level of control over five of six degrees of freedom that has not been demonstrated with other trapping techniques. Here, using photonic crystal resonators, the manipulation of microtubules and carbon nanotubes was demonstrated by studying the dynamics of the orientation in the dipole moment framework. The action of the electromagnetic field on nanorods was described as a torsion spring and the torsion spring constants were determined to 92.8 pN·nm/rad^2-mW for MTs and 22.8 pN nm/rad^2-mW for MWCNTs. Additionally, he rotational diffusion rate was observed to be reduced 3.7 times for a trapped MT compared to a freely diffusing one. We believe such tight grasp on biological and non-biological material should enable novel biophysical studies and find use in nanoscale assembly and material sciences.

Chapter 5

A PHOTONIC CRYSTAL RESONATOR

5.1 Abstract

Near-field optical resonators based on photonic crystals have allowed optical manipulation at single molecular level such as proteins and DNA. In design and fabrication of photonic crystal based optical resonators, silicon nitride material provides a few advantages to silicon including working wavelength and deep penetration depth of the evanescent field. However design requirement of high quality factor using nitride materials causes relatively low intensity of electromagnetic field by large scattering loss from photonic crystal structures. Here we present design of a nitride photonic crystal resonator that provides large optical force resulting from less scattering loss. In addition, using less number of cavities reduces fabrication variations.

5.2 Introduction

We have demonstrated near-field optical manipulation techniques that can handle nanoscale particles and biomolecules (D ~10s nm) such as proteins, quantum dots, and DNA[67], so as to overcome a size limitation on the manipulation by conventional optical tweezers (D ~100s nm)[20,21]. However the quality factor of the photonic crystal (PhC) resonator was lower than what was expected in the design. It was found that varying sizes of over a hundred of mirror cavities caused fabrication variations in fabrication processes, leading to poor performance of devices. The variations also caused deviation of working wavelength from 1064 nm. This leads to relatively small optical trap force resulting from less coupled intensity of light to a

resonant cavity. Thus we have simplified the sophisticated design with a trade-off between a quality factor and a geometric simplicity.

5.3 Design and Fabrications

First we used a general design principle[18] to systematically design a photonic crystal resonator. More specifically, we conducted finite-difference time-domain analysis (Lumerical Solutions, Inc.) to numerically verify and optimize the design parameters including cavity diameters, periodic separation length, and cavity length. Geometries figured out to be D = 178 nm, a = 352 nm, L_{cav} = 1.5a, and N_{cav} =25 for each side of an optical mirror made of photonic crystal systems, which is also called a Bragg mirror. The designed resonator was fabricated by procedure briefly described in the following.

NEB-31 electron beam photoresist was spun on a wafer on which a 250-nm stoichiometric silicon nitride layer was deposited on top of a 3.5 μm thermal oxide layer by low-pressure chemical vapor deposition (LPCVD). To reduce a charging effect during exposure, a 5-10 nm thin gold film was deposited on the resist with a thermal evaporator. It was patterned using a JEOL 9500 electron beam lithography system. A patterned wafer is processed with lift-off to coat with a 3.5 m thermal oxide layer except resonator regions for protection of chips and waveguides. Lastly, it was diced in approximately 5 × 1 centimeter chip to construct microfluidic channels on top of a chip. A microfluidic chamber allows flowing and switching solutions so that fluidic control is integrated to develop a new method of molecular interaction detection in the following chapter.

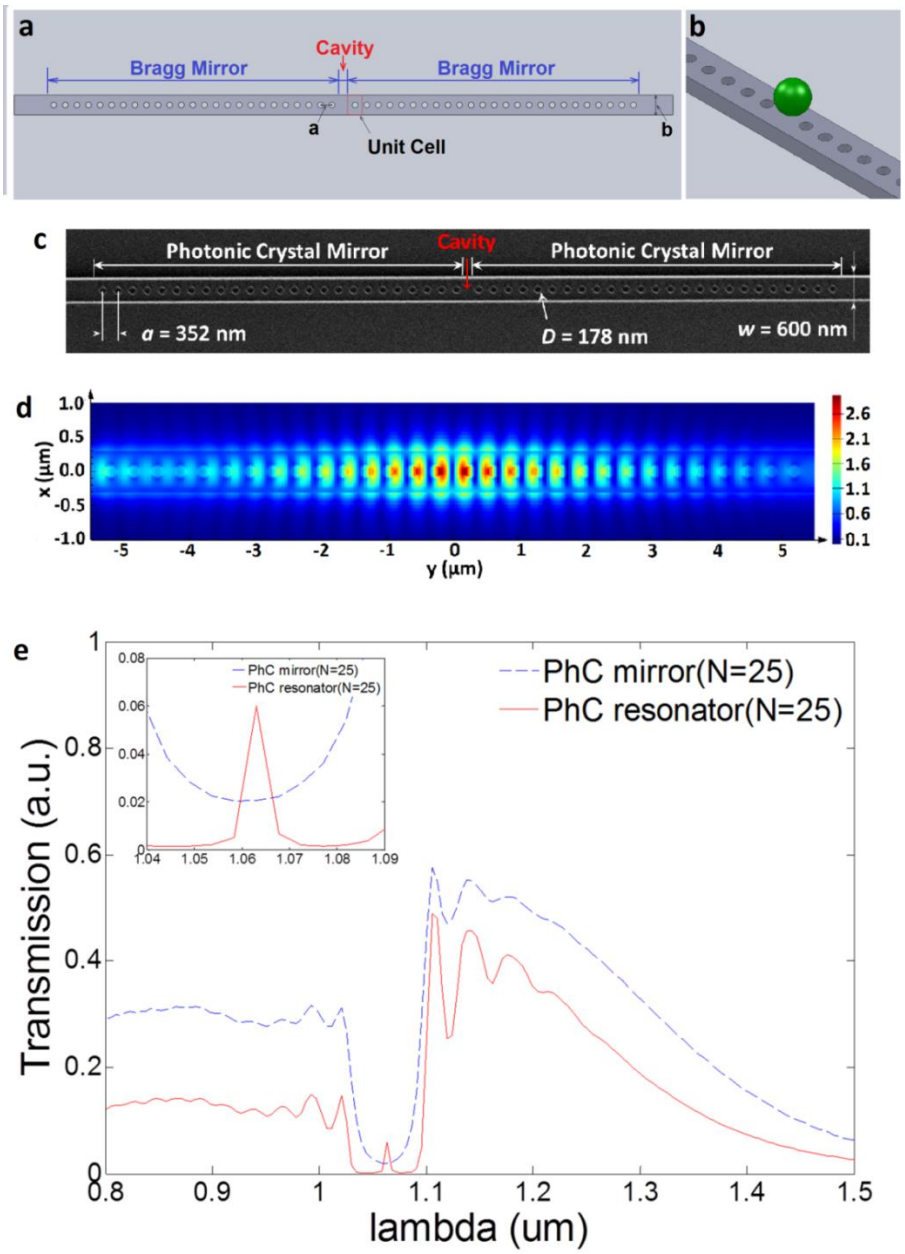

Figure 16 (a) Schematics of geometry of the photonic crystal (PhC) resonator (b) Schematics of optical trapping of a nanoparticle. (c) SEM image of the photonic crystal resonator. (d) FDTD simulation of electric field distribution in the middle plane of the resonator. (e) Simulated transmission spectrum of a Bragg mirror (a red curve) and the resonator (a blue curve). (Inset: Magnified spectrum near λ_{res} = 1064 nm.)

Figure 16 (a) shows the schematics of the proposed resonator structure. It consists of two mirrors for which each has the same number of holes in constant radii with a constant period *a* between holes' center, as well as a cavity length *L* in the center where a particle is trapped as shown in Figure 16 (b). The holes are etched into a ridge waveguide with width *b*. The fabricated PhC resonator was shown in the SEM image of Figure 16 (c). The optimized design provides an electric field distribution shown in Figure 16 (d), which gives rise to a large optical trapping force so as to manipulate the mentioned particles. Figure 16 (e) shows transmission spectrum to be used to determine the Q-factor, which was estimated 436 for the optimized design. In the next step we fabricate a device and examine the quality factor to demonstrate that it matches with the analytical design.

5.4 Conclusions

We have presented the detailed design and fabrication process of photonic crystal resonators that provide large optical force as a result of reduced fabrication variations. The fabricated resonators are expected to be a reliable device, being developed into a biosensor as well as an optical manipulation tool.

Chapter 6

NANOPHOTONIC DETECTION OF FREELY INTERACTING MOLECULES ON A SINGLE INFLUENZA VIRUS

6.1 Abstract

Understanding biomolecular interactions is fundamentally important in the life sciences. Numerous methods[81-85] are currently used to analyze these interactions. However, common approaches[14-16] typically require immobilizing one or both the interacting molecules on an assay plate or a sensor surface, constraining their active binding. When one of the interacting biomolecules is much larger than the other and multivalent, for example a virus and an antibody, this restriction prevents a precise measurement of their affinity and binding capacity[86]. Here we demonstrate a label-free method for measuring the binding affinity and stoichiometry of free-solution interactions between antibodies and single influenza viruses at the attogram scale using near-field optical techniques[26,28,67,87]. By trapping but not immobilizing a virus using a photonic crystal resonator, we detect specific binding by analyzing changes in the confined Brownian motion of the virus. In addition, our detection relies upon evanescent wave light scattering for analyzing the Brownian motion, allowing the label-free method. Our technique can be applied to a wide range of molecular interactions because the nanophotonic tweezer can handle molecules with sizes ranging from tens to thousands of nanometers. Additionally, this technique can provide quantitative information about the potential pathogenicity or the virulence of a virus.

6.2 Introduction

Investigating interactions between a pathogenic virus and its antibody plays a key role in pathogen control and prevention. It allows identification of the pathogen type and determination of the virulence. A number of optical[8,88], electrochemical[89,90], and mechanical[91] techniques have been developed for the detection of single viruses. In addition to detection, recently developed imaging-based techniques[7,92,93] are capable of giving quantitative information such as the size and mass of single viruses. These methods enable label-free detection, but they rely on immobilizing a specific antibody on a sensing area and thus constrain the active binding to the virus. As a result, the binding kinetics measured using these techniques may not be representative of what occurs in free solution[17].

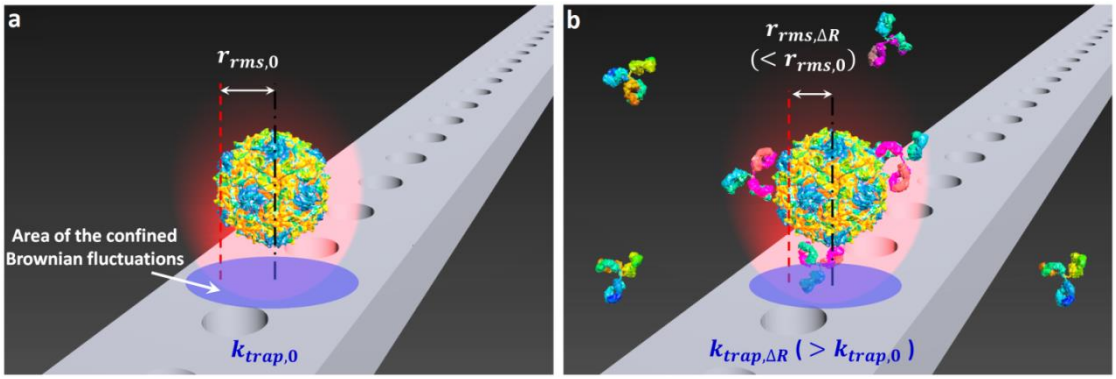

Figure 17 Detection principle for label-free detection of binding interactions between an influenza virus and antibodies. (i) A single influenza virus is captured in a nanophotonic near-field trap (ii) Detection of binding of an anti-influenza antibody to the virus within the optical trap. The analysis of the Brownian fluctuations determines the decreased r_{rms} (or increased k_{trap}) resulting from the bindings. Note that subscript 0 denotes an initial measurement, and subscript ΔR denotes the measurement at equilibrium.

In this paper we present a method that detects unrestricted interactions between biomolecules. Using a near-field optical trap,[67] this technique provides quantitative analysis of the interactions at the attogram scale. Briefly, this method exploits the fact that the optical force exerted on a trapped particle is proportional to the particle's volume and polarizability[22]. The spring constant or the trap stiffness can be extracted from the Brownian fluctuation of the trapped particle[22]. Thus, by observing these fluctuations, we can detect the binding of a partner biomolecule to the trapped particle (Figure 17). This enables us to detect the binding interactions without restricting them by immobilizing or labeling either of interacting biomolecules. In addition, the model that we have developed for the effective polarizability of the binding complex enables accurate measurements of the affinity and stoichiometry of the interactions (Figure 17a – i and ii). In this paper, we first characterize the method using an antibody binding assay in which one interacting antibody is coupled to the surface of a nanoparticle and the partner antibody freely moving in a solution binds to it. This assay shows that our detection method is reliable by comparing our measured affinities and stoichiometries to known values. Next, we demonstrate binding interactions where neither of the interacting biomolecules is immobilized. We detect the binding of antibody to a single human influenza A virus, and measure stoichiometry of the specific antibody. In this demonstration, we perform the assay in a label-free manner using a near-field light scattering technique to monitor the position of the virus[87].

6.3 Analytical Model

We describe the result of molecular binding to the target using an effective sphere model of antibody-particle complexes (Fig. 18a – i and ii). The effective polarizability of the sphere allows us to describe the interactions with the known applied optical force from the equation[22,28] $F_{trap} = 2\pi\nabla I_o(z)\alpha_{eff}/c$, where, c and λ are the speed and wavelength of light, $I_o(z)$is the incident intensity on a trapped particle, and α_{eff} is the effective polarizability[94] expressed as below.

$$\alpha_{eff} = 4\pi\varepsilon_0\left(\frac{\varepsilon_e - \varepsilon_m}{\varepsilon_e + 2\varepsilon_m}\right)R_{outer}{}^3 \tag{11}$$

$$\varepsilon_e = \varepsilon_s\left(\frac{R_{outer}{}^3(\varepsilon_c + 2\varepsilon_s) + 2R_{inner}{}^3(\varepsilon_c - \varepsilon_s)}{R_{outer}{}^3(\varepsilon_c + 2\varepsilon_s) - R_{inner}{}^3(\varepsilon_c - \varepsilon_s)}\right) \tag{12}$$

where ε_c, ε_s, and ε_m are the dielectric constants of the core (polystyrene or a virus), shell (antibodies), and medium (water) respectively, ε_e is the effective dielectric constant of the core-shell complex ($\varepsilon \approx n^2$ assuming non-absorbing materials of refractive indices such as 1.59 for a polystyrene (PS) particle, 1.41 for an antibody[16], and 1.48 for an influenza virus[93]), R_{outer} is the core-shell radius, and R_{inner} is the core radius. The force is calibrated with its spring constant or the trap stiffness[22].

In our experiments, we optically trap a particle using a photonic crystal (PhC) resonator (Figure 18b – i and ii, and Supplementary Information). We use the Equipartition method[95] to extract the trap stiffness from the positional variance of the particle within the optical trap using video tracking analysis.

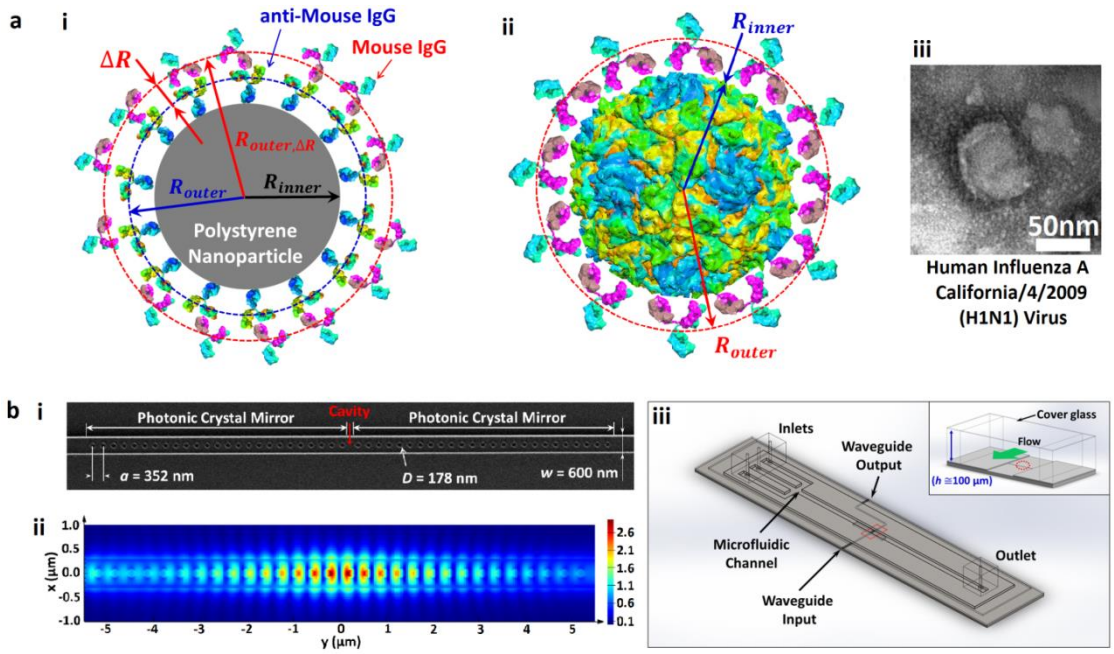

Figure 18 Effective sphere model of antibody-particle complexes and the nanophotonic tweezer (a) Schematic of detecting interaction between an influenza virus and antibodies. (i) Optical trap of a single influenza virus (ii) Detection of specific binding of an anti-influenza antibody to the virus within the optical trap (b) (i) A core-shell model of a goat anti-mouse IgG-coated polystyrene particle and bound mouse IgGs to the anti-mouse IgGs. (ii) A core-shell model of a virus and bound antibodies. Viral envelope is not shown for simplicity. (iii) A TEM image of an influenza virus (see Methods). (c) (i) SEM image of the photonic crystal resonator. (ii) 3D FDTD simulation illustrating the strong field confinement within the resonator cavity. (iii) 3D schematics of an integrated optofluidic device. The inset shows a cross sectional view noted with a red box.

Next we obtain the relationship between the change in the particle radius and the trap stiffness. We relate the relative trap stiffness of the complex after binding to that of the particle before binding with the relative polarizabilities expressed as $(k_{trap,\Delta R} / P_{\Delta R}) / (k_{trap,0} / P_0) = \alpha_{eff,\Delta R} / \alpha_{eff,0}$, where P is the power, k_{trap} is the trap stiffness, subscript 0 denotes an initial measurement, and subscript ΔR denotes the measurement at equilibrium. Therefore, if we know refractive indices of the trapped particle and binding antibody, we can detect specific binding characterized by the change in radius corresponding to the bound layer, ΔR, by measuring the relative trap stiffness. This relationship is described by the transcendental equation,

$$R_{outer,\Delta R} = R_{outer} + \Delta R = \left[\frac{\left(\frac{k_{trap,\Delta R}}{P_{\Delta R}} \right)}{\left(\frac{k_{trap,0}}{P_0} \right)} \cdot \frac{\left(\frac{\varepsilon_{e,0} - \varepsilon_m}{\varepsilon_{e,0} + 2\varepsilon_m} \right)}{\left(\frac{\varepsilon_{e,\Delta R} - \varepsilon_m}{\varepsilon_{e,\Delta R} + 2\varepsilon_m} \right)} \right]^{1/3} \cdot R_{outer} \qquad (13)$$

where $k_{trap} = 2k_B T / r_{rms}^2$, where k_B is the Boltzmann constant, T is the temperature in K, and $r_{rms}^2 = (1/n)\sum(x^2 + y^2)$ is the variance of n instantaneous positions[96] and all other variables are noted as previously (see Supplementary Information for detailed derivation).

6.4 Results and Discussion

To validate our technique we first measure specific binding between a fluorescent polystyrene bead coated with goat anti mouse IgG and antibodies in solution. We compare our measured binding capacity of antibodies with the manufacturer's quoted value (Spherotech Inc.). The position fluctuations are measured

using fluorescence microscopy (Figure 19a). Typical measurements are shown in Figure 19b.

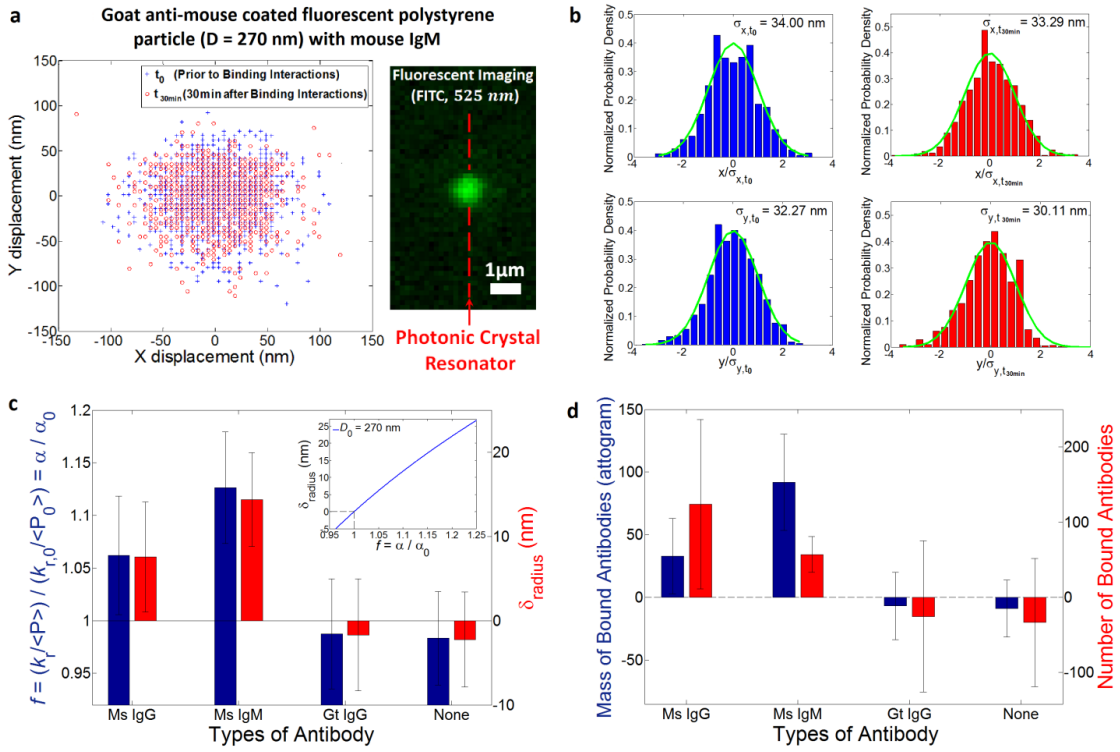

Figure 19 Biding of antibodies to goat anti-mouse IgG coated on the surface of fluorescent polystyrene particle ($D_{mean} \approx 270$ nm) (a) Tracking trajectories within the optical trap before (blue crosses) and after (red circles) the binding with mouse IgM. The image on the right side captured by a CCD camera shows a IgG-coated colloid trapped at the resonator cavity. (b) Probability density histograms of x (top) and y (bottom) displacements before (left, blue bars) and after (right, red bars) bindings with mouse IgM. Green curves are Gaussian fits to the histograms. Data are representative of all experiments. (see Supplementary Information (SI)) (c) Measured relative power-normalized trap stiffness and radius increases for different solutions of mouse IgG (N = 3), mouse IgM (N = 4), and goat IgG (N = 3), and a buffer (N = 5). N represents a number of independently performed experiments. The inset exhibits an analytical plot of the radius change to the relative polarizability for a IgG-coated colloid with D_0 = 270 nm. (d) Stoichiometries of the antibodies to the colloid. All error bars are determined by $(\sum \sigma_f{}^2)^{1/2}/N$ (see SI for details on σ_f, standard deviation of an independent experiment).

Changes in power-normalized trap stiffness and radius increases of an IgG coated colloid are compared for solutions of mouse IgG, mouse IgM, goat anti-rabbit IgG, and a buffer (Figure 19c). Again, we use Equation (13) to correlate the power-normalized relative trap stiffness to the radius increase with a known initial diameter for R_{outer} ($D \approx 270$ nm, Figure 19c inset). From studies on protein sizes[14,97,98] we predict changes in thickness resulting from specific antibody binding to be 5.79 nm for IgG ($M_{\mathrm{IgG}} = 160.5$ kDa) and 10.55 nm for IgM ($M_{\mathrm{IgM}} = 970$ kDa). Affinity is indicated by a measured radius increase 7.5 ± 6.5 nm and 14.4 ± 5.6 nm for solutions of mouse IgG and mouse IgM respectively, in agreement with our predictions. It should be noted that theoretical estimates are based on the unhydrated mass of protein while in the experiment there are water molecules bound to the antibody. Electrical measurements by Saleh *et al.*[90] indicate an increase of about 4.5 nm for IgG. Specificity is demonstrated by measured negligible radius increases of -1.7 ± 6.6 nm and -2.2 ± 5.7 nm in the solution of an unspecific antibody (goat anti-rabbit IgG) and a buffer respectively.

Figure 19d shows the stoichiometry of each binding event. The manufacturer-quoted binding capacity of coated IgG to polystyrene particles (Spherotech, Inc) is ≈ 117.4 IgGs (≈ 31.3 *ag*) per particle. The manufacturer-quoted binding capacity of mouse IgG (FITC-labeled) to coated anti-mouse IgG is ≈ 107.6 IgGs (≈ 28.7 *ag*) per particle. In comparison, the binding capacity measured in our affinity assay for mouse IgG was 124.0 ± 112.7 IgGs (33.0 ± 30.0 *ag*) per particle, whereas for mouse IgM it was 57.0 ± 23.9 IgMs (91.8 ± 38.5 *ag*) per particle. Despite the large uncertainties, our results of the binding capacity indicate a 1:1 binding ratio, consistent with the manufacturer-

quoted binding capacity. Slightly larger binding capacity of the mouse IgG than the manufacturer-quoted one is likely because of unlabeled antibodies used in our experiments. (For details about the uncertainty calculation, see Appendices C.6).

Next we demonstrate detection of the specific antibody to a human influenza A virus using the near-field light scattering technique[87] (Figure 20a). The technique allows us to develop our detection method for pathogen identification without the need of labeling either of a virus or an antibody. In this assay we demonstrate that our method can accurately measure affinity and stoichiometry of an anti-influenza antibody to the influenza virus. Moreover we show that the sensitivity of the binding detection can be improved by trapping a smaller target particle like an influenza virus ($D \approx 100$ nm) than a 270-nm diameter IgG coated colloid (Figure 20b).

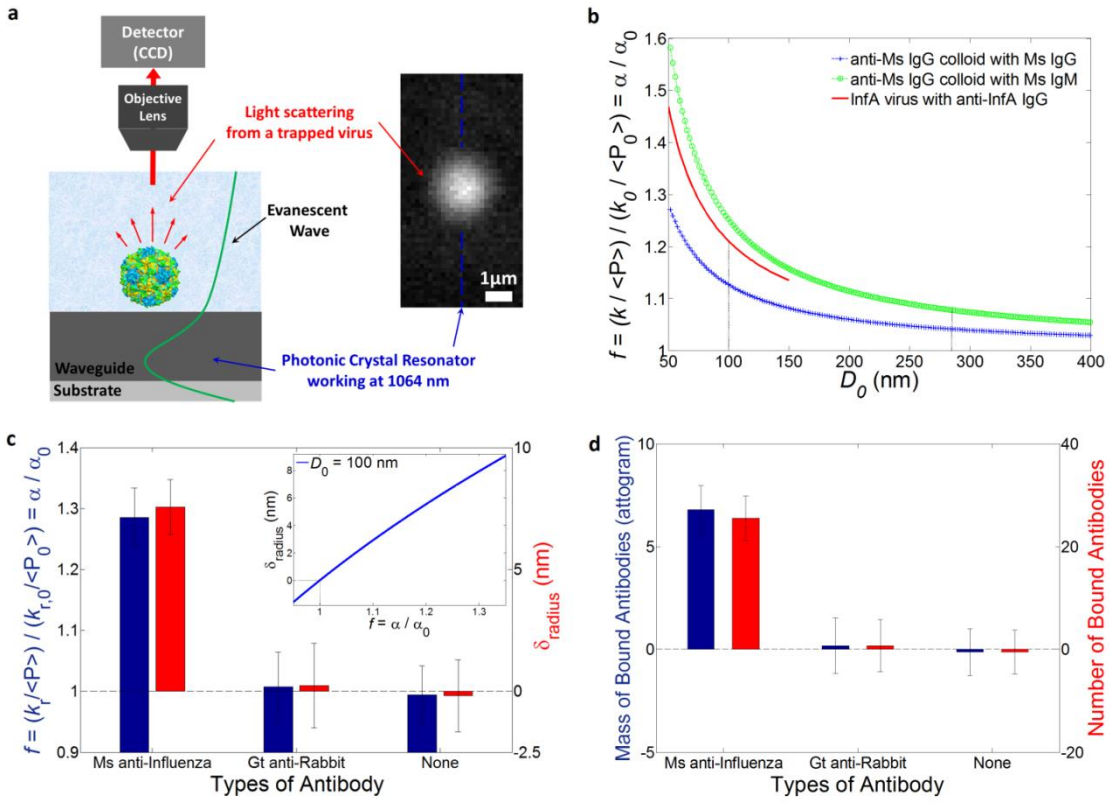

Figure 20 Binding of antibodies to a human influenza A H1N1 virus ($D_{mean} \approx 100$ nm). (a) Experimental setup of the light scattering imaging. The inset shows a trapped virus particle ($D_{virus} \approx 100$ nm). (b) Analytical plot of predicted relative power-normalized trap stiffness to varying size of different binding complexes (see SI for more details) (c) Measured relative power-normalized trap stiffness and radius increases for different solutions of mouse anti-influenza IgG ($N = 3$) and goat anti-rabbit IgG ($N = 3$), and a buffer ($N = 3$). N represents a number of independently performed experiments. The inset shows an analytical plot of the radius change to the relative polarizability for an influenza virus with $D_0 = 100$ nm. (d) Stoichiometry of the antibodies to the influenza virus. All error bars are determined by $(\sum \sigma_f^{\,2})^{1/2}/N$ (see SI for details on σ_f).

Changes in power-normalized trap stiffness are compared for different solutions of mouse anti-influenza IgG, goat anti-rabbit IgG, and a buffer (Figure 20c). Again, we use Eq. 2 to correlate the power-normalized relative trap stiffness to the radius increase with a known initial diameter for R_{inner} ($D_{virus} \approx 100$ nm, Fig. 3b inset). Affinity is indicated from a radius increase 7.6 ± 1.1 nm in the solution of mouse anti-influenza IgG. We attribute the radius increase to the specific binding of anti-influenza IgG. Specificity is demonstrated by much smaller radius increases 0.2 ± 1.7 nm and -0.2 ± 1.5 nm in the solution of an unspecific antibody (goat anti-rabbit IgG) and a buffer respectively. Compared to the previous assay, the sensitivity of binding detection to the unspecific binding was improved. We attribute this not only to smaller size of viruses than the colloids but to less thermal noise from the light scattering imaging than the fluorescence imaging (see Supplementary Information for more details).

Figure 20d shows the stoichiometry of the binding antibodies. The binding capacity of anti-influenza IgG to the virus is 6.8 ± 1.1 *ag* (25.5 ± 4.3 IgGs) per virus. In comparison, specificity is shown by much smaller binding of 0.2 ± 1.4 *ag* (0.7 ± 5.1 IgGs) and -0.1 ± 1.1 *ag* (-0.5 ± 4.3 IgGs) per virus in the solution of goat anti-rabbit IgG and a buffer respectively. We do not provide comparison of our measurement of this stoichiometry because there is no available previous analysis to compare to directly. While many recently developed techniques[7,8,82-84,88,93,99] are capable of virus detection, our technique enables quantitative measurements of the binding capacity of an anti-influenza antibody to a single virus.

6.5 Conclusions

We have demonstrated a method to directly and accurately detect the binding of unrestricted biomolecules using near-field optical trapping. We have also shown the capability to measure the affinity and stoichiometry of biomolecular interactions at the attogram scale. Our measurements of the affinity and the stoichiometry of the specific antibody to the colloid were in good agreement with the manufacturer-quoted binding capacity. Our detection method does not require labeling or immobilizing either of the interacting biomolecules. We report the first affinity measurements for a single influenza virus and an anti-influenza antibody, which was found to be 6.8 (± 1.1) attogram of anti-influenza antibodies per virus. Our method can be utilized for studying the potential pathogenicity and virulence of rapidly mutating influenza viruses in addition to identification. Furthermore, our light-scattering-based detection method can be used to monitor biomolecular interactions in real time, giving new information on the kinetics of the interaction at a single molecule level. This technique has many potential applications both in drug discovery for screening and developing drug compounds and in clinical diagnosis as a label-free ultrasensitive biosensor.

Chapter 7

CONCLUSIONS

7.1 Summary

The goal of this dissertation was developing nanophotonic techniques using photonic crystals. The photonic crystal structures have been utilized to construct a three dimensional photonic crystal substrate with a self-assembling technique. The technique has eased the fabrication of photonic crystal structures using subwavelength-sized colloids whose size is on the order of visible wavelengths. The colloidal photonic crystal substrates have been used to obtain high-resolution images as fine as 200 μm with transparent inks. The inks have allowed for multicolor images that are erasable with low vapor pressure silicon oil.

The photonic crystal structures have been integrated in an optical waveguide to develop a photonic-crystal-based optical resonator. The photonic crystal resonator has been employed to develop optical manipulation techniques, including near-field optical trap, transport, and handling Rayleigh-sized biological molecules such as viruses and proteins. The near-field-based optical manipulation techniques have allowed handling of biomolecules in a few tens of nanometers below a hundred nanometers. Traditional optical tweezers manage to deal with the size range with high power that causes optical damage to biomolecules.

The near-field optical manipulation techniques have been extended to enable the control of angular orientation of rod-like materials, including microtubules and carbon nanotubes. The study of the dynamics of orientation has discovered that the polarized TE mode in the photonic crystal resonators induced optical torques of 92.8

pN nm/rad^2-mW for microtubules and 22.8 pN nm/rad^2-mW for multi-walled carbon nanotubes. The torque has shown the possibility of angular optical trap that restricts the degree of freedom in angular Brownian diffusion motions.

Further development of nanophotonic techniques has provided a novel method for the label-free measurement of biomolecular interactions. The method has shown affinity measurements for a single influenza virus and an anti-influenza antibody, which was determined to be 6.8 ($\pm$ 1.1) attogram of anti-influenza antibodies per virus. The optical manipulation of single viruses, along with near-field light scattering imaging and microfluidic techniques, has created a new method that does not require labeling or immobilizing either of the interacting biomolecules.

7.2 Future outlook

Photonic-crystal-based technologies have a wide range of applications that can be developed based on what has been demonstrated here. The colloidal photonic crystal structure used has been integrated in polydimethylsiloxane (PDMS) material because silicon oil is capable of infiltrating the material which leads to an increase in volume. If smart materials sensitive to temperature, light, electric signal, and toxic materials are used as a matrix material, the photonic crystal substrate can be developed for colorimetric sensors that respond to external stimuli. For future work, a technique is needed to obtain uniformity of the photonic substrate on a larger scale.

This demonstration of handling single biomolecules shows the possibility that near-field optical manipulation techniques with angular control can be employed to build nano-assemblies such as three dimensional structures with DNA bricks[4]. The

built structures can be developed into a nanorobot for targeted delivery[11]. In addition to the near-field nanomanipulation techniques, the microfluidic control method will be required to make complicated structures.

Furthermore, the molecular interaction measurement method can be developed into a technique that performs real-time biomolecular interaction monitoring with near-field light scattering imaging. The developed method will enable new discoveries about the kinetics of biomolecular interaction in a wide range of biological systems, especially for multivalent bindings. This technique will also have an impact in drug discovery for screening and developing drug compounds as well as in clinical diagnosis, if the systems integrate with high throughput.

Appendices

Chapter 3

A. Fabrication of colloidal photonic crystal substrates

The procedure for creating self-assembled colloidal photonic crystal (CPC) substrates can be found in earlier publications[51,53]. Here the CPC substrates are fabricated from monodisperse polystyrene (PS) nanospheres (Polysciences, Inc) 200 nm in diameter dispersed at 25mg/ml in pure water. Glass slides used to perform the assembly were first cleaned in 95% sulfuric acid for an hour to remove organic residues and make surfaces hydrophilic. Next the glass slides are rinsed with Acetone, 2-propanol (IPA), and DI water. To further increase the wettability, the glass slides are treated with oxygen plasma (Harrick Plasma) for one minute. To initiate the assembly process, 3ml of the PS dispersion solution was dispensed on the glass slides and then immediately covered with silicone oil (Gelest, Inc., Polydimethylsiloxane DMS-T11, η=10cSt) to slow the evaporation process enabling long-range order to be obtained. Substrates were placed in an oven at 60℃ for several days while the assembly proceeded. After the water was completely evaporated, the silicon oil was carefully cleaned off. Premixed PDMS (1:1 mixture of PDMS base (Sylgard 184) and silicon oil (Gelest, Inc., Polydimethylsiloxane DMS-T00, η=0.65cSt)) was then poured over the substrate allowing it to infiltrate into the interstitial spaces in the crystal.

Chapter 4

B. Materials and Methods

B.1 Preparation of microtubules

For the orientation experiment with microtubules, porcine brain tubulin protein is used to form the microtubule. The tubulin protein is labeled with TRITC rhodamin. The TRITC rhodamine labeled tubulin protein (Cat. # TL590M) is supplied from Cytoskeleton Inc. Denver, CO. USA. The microtubules were re-incubated with Paclitaxel (Cat. # TXD01) between 30 minutes to an hour prior to the experiments.

B.2 Preparation of the multi-walled carbon nanotube

Carbon nanotubes suspensions were prepared by ultrasonification of 0.01% MWCNT powder (7-15 nm OD, Sigma-Aldrich product # 694185, and 110-170 nm OD, Sigma-Aldrich product # 659258) and 0.5 % Tween-20 (Sigma-Aldrich Product # P1379) in heavy water.

B.3 Fabrication of the Silicon Nitride and Silicon PhC resonator[67]

The fabrication of the silicon photonic crystals and silicon nitride photonic crystals was performed with standard E-Beam lithography in the CNF. Additional information is available in references 13 and 14. The design of the resonators followed the method developed by Quan *et al*[18])

B.4 Flow Cell Preparation

To flow the nanorods, the flow compartment is made on the fabricated device. 127 μm-thick parafilm spacer that has 2 mm-width flow channel is placed on the device such that the flow channel is placed on the resonator. Inlet and outlet holes were made on a coverslip using the Universal Laser Systems, VersaLaser VLS3.50. PDMS pieces to fix Tygon tubuing in the holes were attached on the coverslip. The coverslip is then placed on the top of the parafilm spacer. The entire sandwiched components were briefly heated on hotplates at 80℃ to make sealed compartment. The flow compartment was estimated to be approximately 2 mm×100 μm as the cross-section. In orientation experiments, the sample is injected into the compartment through Tygon tubing by a syringe pump. Prior to experiments, washing buffer solution of PBS, Tween20 (0.05% w/w), and Casein (0.05% w/w) was incubated for 30 minutes to wash the surface of the resonator and prevent nonspecific binding.

B.5 Orientation Experiments

For a light source a 1064 nm fiber coupled high power diode laser (LU1064M400 Lumics, EL Segundo, CA) was used to achieve optical orientation and optical trapping. A laser power was controlled by a laser diode controller, THORLABS ITC 502 combined with a temperature control. The temperature of a laser diode was adjusted to tune the center wavelength of the laser diode such that slightly dissimilar resonance wavelength of resonators resulted from fabrication is compensated. The Laser light was coupled into silicon nitride waveguides through a lensed fiber. The power coupled to the resonator was measured by a detector of a

power meter aligned with output of waveguides. Polarization of a laser light was controlled to be transverse electric (TE) mode with a polarizer and a manual fiber polarization controller through which a fiber passes. The measured power was to reach maximum during control. Images were captured and recorded with an upright fluorescent microscope, Olympus BXFM system equipped with a Hamamastu ORCA-ERCCD camera. To excite the fluorescence of TRITC labeled microtubules, a mercury arc lamp was used with a TRITC filter set.

B.6 Image processing and Data analysis

Image analysis of the orientation and the Brownian motion of nanorods were performed using ImageJ[66]. OrientationJ[74] was used to measure the orientation angle quantitatively. The standard deviations of the measured orientation angles were affected by imaging quality with a 10-15% error.

Chapter 6

C.1 Design and fabrication of a photonic crystal resonator

Device design was performed by three dimensional FDTD simulation using FDTD solutions (Lumerical Solutions Inc.). Device fabrication is followed by the procedure presented by Chen *et al.*[67] (see its supplementary information) with following changes. NEB-31 electron beam photoresist was spun on a wafer on which a 250-nm stoichiometric silicon nitride layer was deposited on top of a 3.5 μm thermal oxide layer by the low-pressure chemical vapor deposition (LPCVD). To reduce a charging effect during exposure, a 5-10 nm thin gold film was deposited on the resist with a thermal evaporator. It was patterned using a JEOL 9500 electron beam lithography system.

C.2 Experimental Setup

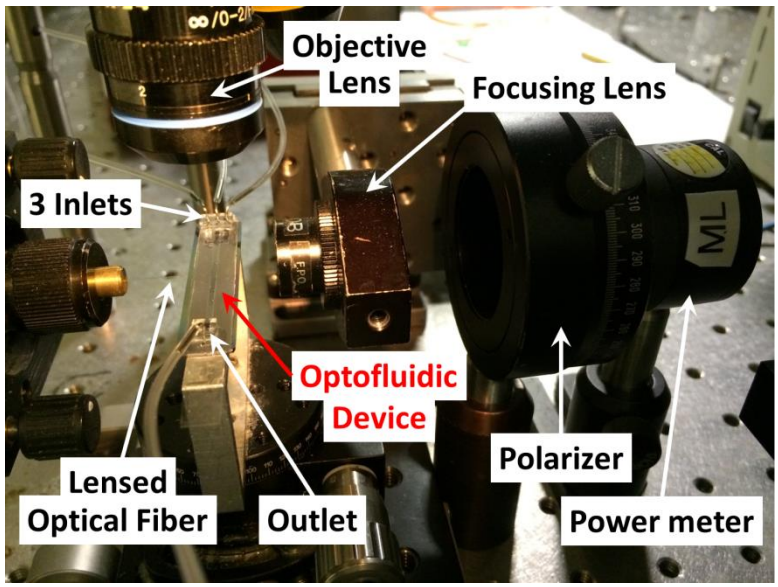

Figure 21 Illustration of an experiment setup. 1064nm diode laser is connected to a lensed optical fiber. Optical coupling is carried out by alignments: output waveguide, a focusing lens, a polarizer, and the detector of a power meter.

A 1064 nm fiber coupled diode laser (LU1064M400, Lumics, El Segundo, CA) was used as a light source for optical trapping. The laser was coupled to the input waveguide of silicon nitride through a lensed optical fiber. A thermistor in the laser diode was controlled to tune in a resonance wavelength of a photonic crystal resonator with an increase of approximately 0.3 nm per 1 K temperature rise. The power coupled into the resonator was measured by focusing the light emitting from output waveguide onto a detector of a power meter. Power measurements with a power meter were sampled in real time using a Labview program. A polarizer passing a TE-polarized light was placed between the focusing lens and the detector.

C.3 Preparation of microfluidic channels

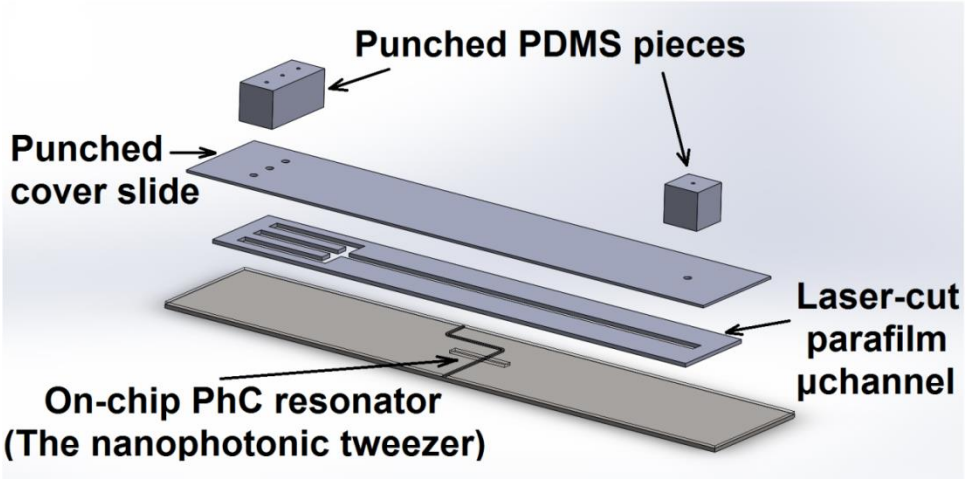

Figure 22 Schematics of microfluidic parts and assemblies. A photonic crystal resonator chip is integrated with microfluidic control systems that inject different solutions and switch between solutions. Three solutions can be infused in inlets whereas waste solution flows into an outlet.

To make flow channels, three holes of D = 500 nm were cut on a glass coverslip using a CO_2 laser (VersaLaser VLS3.50). Punched PDMS piece was bonded to the punched cover glass by oxygen plasma bonding. A 100-μm thick parafilm spacer was cut using the CO_2 laser to have three inlet channels combining to one channel whose width is approximately 1 mm. The parafilm spacer was laid between the cover glass and a fabricated nitride chip. Next the sandwiched complex was briefly heated on a 100-degree-Celsius hot plate to melt the parafilm spacer and bond firmly for preventing leaking in flowing and switching solutions. Tygon tubings were inserted tightly to the holes through PDMS fixtures to inject solutions into the channels using three syringe pumps (Harvard Apparatus, Holliston, MA). Before conducting experiment, a SuperBlock blocking buffer solution (Sigma-Aldrich, 37580) with 0.05% tween 20 (Sigma-Aldrich, P7949) was filled in the channels and incubated either over 30 min at room temperature or over 12 hours at 2-8 degree Celsius to prevent non-specific binding.

C.4 Detailed derivation of the analytical model

To accurately measure affinities and stoichiometries of the interactions, we obtain the relationship between the relative trap stiffness and a radius increase as following. First, we relate the optical force exerted on a non-absorbing ($\varepsilon \approx n^2$) Rayleigh particle to radius of the particle by polarizability α_{eff} as in $F_{trap} = 2\pi\nabla I_o \alpha_{eff}/c$, where α_{eff} is the effective polarizability of the particle, c and λ are the speed and wavelength of light, and I_o is the incident intensity[22,28]. Noting that binding of

biomolecules to the trapped particle changes the polarizability, we describe the change by using the core-shell model of a coated sphere to account for the effective polarizability of dissimilar dielectric constituent materials, for example, antibodies and polymer (Fig. 1e - i), and antibodies and virus (Fig. 1e - ii) in our assays, expressed as

$$\alpha_{eff} = 4\pi\varepsilon_0 \left(\frac{\varepsilon_e - \varepsilon_m}{\varepsilon_e + 2\varepsilon_m} \right) {R_{outer}}^3 \tag{14}$$

$$\varepsilon_e = \varepsilon_s \left(\frac{{R_{outer}}^3(\varepsilon_c + 2\varepsilon_s) + 2{R_{inner}}^3(\varepsilon_c - \varepsilon_s)}{{R_{outer}}^3(\varepsilon_c + 2\varepsilon_s) - {R_{inner}}^3(\varepsilon_c - \varepsilon_s)} \right) \tag{15}$$

is the effective dielectric constant of the sphere, ε_c, ε_s, and ε_m are the dielectric constants of the core, shell, and medium respectively, R_{outer} is the core-shell radius, and R_{inner} is the core radius[94]. Thus we relate the change in the polarizability to the change in size using the equation (14).

Second, we use the Equipartition theorem to determine the optical force by measuring position fluctuations of the trapped particle. It is noted that the optical force is modelled as a spring such as $F_{trap} = k_{trap}\, r$, where k_{trap} is the trap stiffness; k_{trap} is determined by measuring the position fluctuations and using the Equipartition theorem as in $k_{trap} = 2k_BT/{r_{rms}}^2$, where k_B is the Boltzmann constant, T is the temperature in K, and ${r_{rms}}^2 = (1/n)\sum(x^2 + y^2)$ are the variance of n instantaneous positions of the particle[96]. Finally assuming small displacements within the optical trap that gives $k_{trap} = \partial F_{trap}/\partial r$, we obtain the equation that relates the trap stiffness to the effective polarizability such as $k_{trap} = 2\pi\alpha_{eff}\,(\partial^2 I_o/\partial r^2)$, substituting this into the relative trap stiffness $k_{trap,\Delta R}/k_{trap,0}$, that yields $k_{trap,\Delta R}/k_{trap,0} = (\alpha_{eff,\Delta R} / P_{\Delta R})/(\alpha_{eff,0} / P_0)$. Therefore we determine the

radius increase ΔR to detect the specific binding by measuring the relative trap stiffness in experiments with the following transcendental equation.

$$R_{outer} + \Delta R = \left[\frac{\left(\frac{k_{trap,\Delta R}}{P_{\Delta R}} \right)}{\left(\frac{k_{trap,0}}{P_0} \right)} \cdot \frac{\left(\frac{n_{e,0}{}^2 - n_m{}^2}{n_{e,0}{}^2 + 2n_m{}^2} \right)}{\left(\frac{n_{e,\Delta R}{}^2 - n_m{}^2}{n_{e,\Delta R}{}^2 + 2n_m{}^2} \right)} \right]^{1/3} \cdot R_{outer} \qquad (16)$$

where P is the laser power and all other variables are noted as previously.

C.5 Determination of stoichiometry of an interacting antibody

Binding capacity of antibody coated on a polystyrene particle 2.89 μg/mg of particles is used to determine stoichiometry of binding antibody from a radius change. The number of IgG per mg of particle is calculated as $N_{IgG} = M_{IgG,total} / m_{IgG} = 1.084 \times 10^{13}$ IgG/mg, where molecular weight of IgG is 160.5 kDa (= 0.2665 *ag*). The number of polymer particles per mg are calculated as $N_{ps} = M_{ps,total} / m_{ps} = M_{ps,total} / (\rho_{ps} \pi D^2) = 9.241 \times 10^{10}$ particles/mg, where the density of polystyrene is 1.05 g/cm^3, and manufacturer-quoted diameter of particles is approximately 270 nm. Therefore the binding capacity of anti-mouse IgGs to a polymer particle is calculated to be 117.4 IgGs per particle. Volume occupied by the number of antibody ($N_{\mathrm{IgG}} = 117.4$) to the volume of a IgG-coated layer ($t = \delta_{IgG} = 5.794$ nm) determines the antibody density in a binding layer. Volume of an individual antibody is determined from dehydrated mass of an antibody[16,97] as $V = d_{IgG\ (or\ IgM)}{}^3$, where $d_{IgG} = 5.79$ nm and $d_{IgM} = 10.55$ nm. We use the density to determine the volume of antibodies binding to a IgG-coated

colloid with a radius increase resulting from the bindings. This allows us to determine the total mass of bound antibodies, and thus find the number of the bound antibodies.

C.6 Uncertainty of a measurement of the relative power-normalized trap stiffness

The detection method we have developed is based on fluctuation-based measurements that involve external noises such as mechanical vibrations, detector noise, and thermal noise. Determination of the uncertain caused by these factors describes signal-to-noise ratio, providing accurate bioassay analysis. Error propagation of power-normalized trap stiffness is determined to provide error bars in Figure 2 and Figure 3. The relative power-normalized trap stiffness is $f = (k_{\mathrm{trap},\Delta R} / P_{\Delta R}) / (k_{trap,0} / P_0)$, where $k_{trap} = 2\ k_B T / {r_{rms}}^2$ is optical trap stiffness by the Equipartition theorem, P is time-averaged power. Propagation error of f is expressed as

$$\begin{aligned} {\sigma_f}^2 &= \left(\frac{\partial f}{\partial k'}\right)^2 {\sigma_{k'}}^2 + \left(\frac{\partial f}{\partial P'}\right)^2 {\sigma_{P'}}^2 + \left(\frac{\partial f}{\partial k}\right)^2 {\sigma_k}^2 + \left(\frac{\partial f}{\partial P}\right)^2 {\sigma_P}^2 \\ &= f^2 \cdot \left[\frac{{\sigma_{k'}}^2}{k'^2} + \frac{{\sigma_{P'}}^2}{P'^2} + \frac{{\sigma_k}^2}{k^2} + \frac{{\sigma_P}^2}{P^2}\right] \end{aligned} \tag{17}$$

$${\sigma_k}^2 = \left(\frac{\partial k}{\partial T}\right)^2 {\sigma_k}^2 + \left(\frac{\partial k}{\partial \sigma_r}\right)^2 {\sigma_{\sigma_r}}^2 = k^2 \cdot \left[\frac{{\sigma_T}^2}{T^2} + \frac{4^2 {\sigma_{\sigma_r}}^2}{{\sigma_r}^2}\right] = \frac{8k^2}{n-1} \tag{18}$$

$$\sigma_{\sigma_r} = \sigma_r \Big/ \sqrt{2(n-1)} = r_{rms} \Big/ \sqrt{2(n-1)} \tag{19}$$

, where n is the number of instantaneous positions, $\sigma_T \approx 0.4$ K, lead to ${\sigma_T}^2 / T^2 \approx 0$, and σ_p is obtained by a power measurement in experiments. As previously studied[67] low temperature increase of about 0.4 K in a nitride PhC resonator benefits for substantially less thermal noise, as compared to $\Delta k_{trap} \approx 7\%$ resulting from the

fluctuation-based calibration measurement by conventional optical tweezers[100]. Therefore the propagation error of f is estimated by experimentally measurable variables. From measurements the error bar of f is determined from the mean of σ_f for each measurement as $(\sum\sigma_f{}^2)^{1/2} / N$, where N is a number of independently performed experiments. The error bar is statistically nontrivial because it indicates the signal-to-noise ratio of our detection signal f. The error bars of δ_{radius} and stoichiometries are determined from that of f

Typically error of positional variance by a number of $n > 500$ is less than 1% negligible, but it was accounted for estimating total errors with measured power fluctuations σ_p. Especially, approximately 500-900 frames were acquired in each measurement of k_{trap} with fluorescent microscopy at a frame rate, approximately 55-59 frame/sec, allowing 12-20 seconds of observation time for each measurement. The number of frames enabled to avoid thermal noise by fluorescent excitation. In comparison, measurements with the light scattering technique had no restriction on a number of acquired frames, and the number of frames from 1500 to 2000 at the same frame rate as 55-59 frame/sec was obtained for each measurement in a virus affinity assay.

C.7 Supplementary Figures

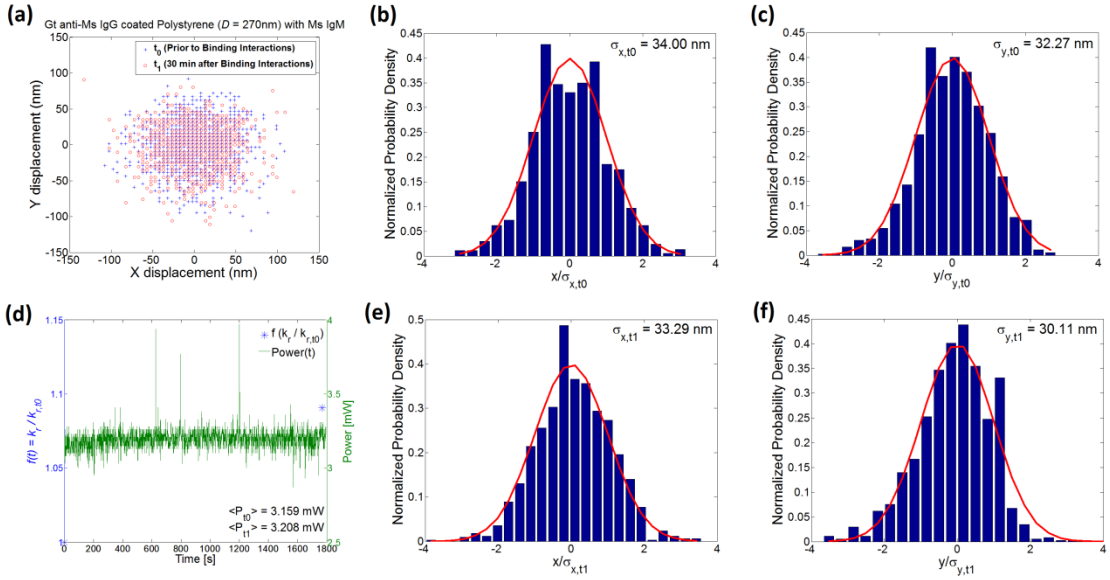

Figure 23 Typical measurements of the optical detection method. (a) Instantaneous positions of the confined Brownian motion within the optical trap before (blue crosses, t_0) and after (red circles, $t_{\Delta R}$) binding interactions. (b) and (c) Normalized probability density histograms of the instantaneous positions in x and y direction, transverse and longitudinal to a waveguide respectively. σ denotes standard deviations of the positions. Red curves show Gaussian fits to the histograms. $k_{x,t0} = 3.4996 \times 10^{-3}$ *pN/nm*, $k_{x,t0} / < P_0 > = 1.6376$ *pN/nm·W*, $k_{y,t0} = 3.8855 \times 10^{-3}$ *pN/nm*, $k_{y,t0} / < P_0 > = 1.8182$ *pN/nm·W*, $k_{r,t0} = 3.6825 \times 10^{-3}$ *pN/nm*, $k_{r,t0} / < P_0 > = 1.7232$ *pN/nm·W* (d) A power measurement over time ($\Delta t = 250$ μs) to normalize the trap stiffness. $< P >$ denotes time averaged power. Power of a TE mode $< P_{TE} >$ is also measured using a polarizer. $< P_{TE,\,t0} > = 2.137$ mW and $< P_{TE,\,t1} > = 2.170$ *mW* in this measurement. (e) and (f) Same histograms as (b) and (c) but at a different time after binding interactions. $k_{x,t1} = 3.6511 \times 10^{-3}$ *pN/nm*, $k_{x,t1} / < P_1 > = 1.7085$ *pN/nm·W*, $k_{y,t1} = 4.4612 \times 10^{-3}$ *pN/nm*, $k_{y,t1} / < P_1 > = 2.0559$ *pN/nm·W*, $k_{r,t1} = 4.0157 \times 10^{-3}$ *pN/nm*, $k_{r,t1} / < P_1 > = 1.8506$ *pN/nm·W*. Note that $<P_{TE}>$ was used for all the power normalization to account for a TE resonance mode in the resonator cavity.

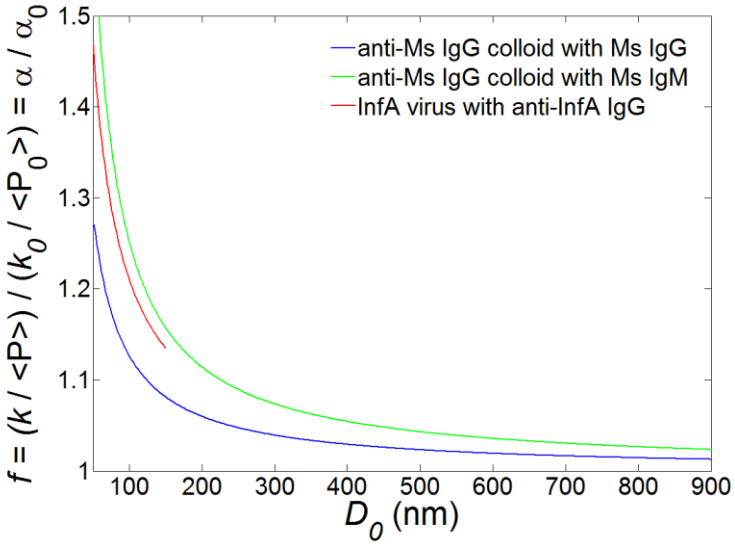

Figure 24 Sensitivity of the detection of bound antibody to different sizes. This analytical plot is calculated from Eq. 2 for varying sizes of R_{inner} and the sizes of antibodies such as IgG and IgM. Following indices n_{PS} = 1.59 for a polystyrene (PS) particle, n_{IgG} = 1.41 for an antibody[16], and n_{virus} = 1.48 for an influenza virus[93] were used for this plot. A blue solid line shows the sensitivity of the detection of bound mouse IgG to a goat anti-mouse IgG coated polystyrene particle whose size ranges in 50 – 900 nm. A green solid line indicates the sensitivity of the detection of bound mouse IgM to the anti-mouse IgG coated colloid whose size ranges in 50 – 900 nm. A red solid line indicates the sensitivity of the detection of bound anti-influenza IgG to a human Influenza A H1N1 virus whose size ranges in 50 – 150 nm. Thickness of bound antibody layers[14,97,98] is considered to be ΔR_{IgG} = 5.79 nm (M_{IgG} = 160.5 kDa) and ΔR_{IgM} = 10.55 nm M_{IgM} = 970 kDa). This graph demonstrates that the sensitivity for detecting the binding of a certain size of a biomolecule increases if the partner molecule priorly trapped is smaller. It is explained from this plot that the sensitivity of the virus assay to detect anti-influenza IgG was higher than that of the characterization assay with the colloid.

BIBLIOGRAPHY

1 Ashkin, A. Acceleration and Trapping of Particles by Radiation Pressure. *Phys Rev Lett* **24**, 156-&, doi:DOI 10.1103/PhysRevLett.24.156 (1970).

2 Ng, L. N., Luff, B. J., Zervas, M. N. & Wilkinson, J. S. Forces on a Rayleigh particle in the cover region of a planar waveguide. *J Lightwave Technol* **18**, 388-400, doi:Doi 10.1109/50.827512 (2000).

3 Ng, L. N., Zervas, M. N., Wilkinson, J. S. & Luff, B. J. Manipulation of colloidal gold nanoparticles in the evanescent field of a channel waveguide. *Appl Phys Lett* **76**, 1993-1995, doi:Doi 10.1063/1.126232 (2000).

4 Ke, Y. G., Ong, L. L., Shih, W. M. & Yin, P. Three-Dimensional Structures Self-Assembled from DNA Bricks. *Science* **338**, 1177-1183, doi:DOI 10.1126/science.1227268 (2012).

5 Lin, C. X. *et al.* Submicrometre geometrically encoded fluorescent barcodes self-assembled from DNA. *Nat Chem* **4**, 832-839, doi:Doi 10.1038/Nchem.1451 (2012).

6 Wei, B., Dai, M. J. & Yin, P. Complex shapes self-assembled from single-stranded DNA tiles. *Nature* **485**, 623-+, doi:Doi 10.1038/Nature11075 (2012).

7 Ignatovich, F. V., Topham, D. & Novotny, L. Optical detection of single nanoparticles and viruses. *Ieee J Sel Top Quant* **12**, 1292-1300, doi:Doi 10.1109/Jstqe.2006.885086 (2006).

8 Vollmer, F., Arnold, S. & Keng, D. Single virus detection from the reactive shift of a whispering-gallery mode. *P Natl Acad Sci USA* **105**, 20701-20704, doi:DOI 10.1073/pnas.0808988106 (2008).

9 Berthelot, J. *et al.* Three-dimensional manipulation with scanning near-field optical nanotweezers. *Nat Nanotechnol* **9**, 295-299, doi:Doi 10.1038/Nnano.2014.24 (2014).

10 Betzig, E. & Chichester, R. J. Single Molecules Observed by near-Field Scanning Optical Microscopy. *Science* **262**, 1422-1425, doi:DOI 10.1126/science.262.5138.1422 (1993).

11 Douglas, S. M., Bachelet, I. & Church, G. M. A Logic-Gated Nanorobot for Targeted Transport of Molecular Payloads. *Science* **335**, 831-834, doi:DOI 10.1126/science.1214081 (2012).

12 Iqbal, M. *et al.* Label-Free Biosensor Arrays Based on Silicon Ring Resonators and High-Speed Optical Scanning Instrumentation. *Ieee J Sel Top Quant* **16**, 654-661, doi:Doi 10.1109/Jstqe.2009.2032510 (2010).

13 Mandal, S., Goddard, J. M. & Erickson, D. A multiplexed optofluidic biomolecular sensor for low mass detection. *Lab Chip* **9**, 2924-2932, doi:Doi 10.1039/B907826f (2009).

14 Gu, H. W., Xu, K. M., Xu, C. J. & Xu, B. Biofunctional magnetic nanoparticles for protein separation and pathogen detection. *Chem Commun*, 941-949, doi:Doi 10.1039/B514130c (2006).

15 Mistrik, P., Moreau, F. & Allen, J. M. BiaCore analysis of leptin-leptin receptor interaction: evidence for 1 : 1 stoichiometry. *Anal Biochem* **327**, 271-277, doi:Doi 10.1016/J.Ab.2004.01.022 (2004).

16 Yu, C. & Irudayaraj, J. Quantitative evaluation of sensitivity and selectivity of multiplex nanoSPR biosensor assays. *Biophys J* **93**, 3684-3692, doi:DOI 10.1529/biophysj.107.110064 (2007).

17 Sulchek, T. *et al.* Single-Molecule Approach to Understanding Multivalent Binding Kinetics. *Ann Ny Acad Sci* **1161**, 74-82, doi:DOI 10.1111/j.1749-6632.2008.04070.x (2009).

18 Quan, Q. M., Deotare, P. B. & Loncar, M. Photonic crystal nanobeam cavity strongly coupled to the feeding waveguide. *Appl Phys Lett* **96**, doi:Artn 203102 Doi 10.1063/1.3429125 (2010).

19 Joannopoulos, J. D., Villeneuve, P. R. & Fan, S. H. Photonic crystals: Putting a new twist on light. *Nature* **386**, 143-149, doi:Doi 10.1038/386143a0 (1997).

20 Ashkin, A. & Dziedzic, J. M. Optical Trapping and Manipulation of Viruses and Bacteria. *Science* **235**, 1517-1520, doi:DOI 10.1126/science.3547653 (1987).

21 Ashkin, A., Dziedzic, J. M. & Yamane, T. Optical Trapping and Manipulation of Single Cells Using Infrared-Laser Beams. *Nature* **330**, 769-771 (1987).

22 Svoboda, K. & Block, S. M. Biological Applications of Optical Forces. *Annu Rev Bioph Biom* **23**, 247-285, doi:DOI 10.1146/annurev.bb.23.060194.001335 (1994).

23 Juan, M. L., Righini, M. & Quidant, R. Plasmon nano-optical tweezers. *Nat Photonics* **5**, 349-356, doi:Doi 10.1038/Nphoton.2011.56 (2011).

24 Righini, M., Zelenina, A. S., Girard, C. & Quidant, R. Parallel and selective trapping in a patterned plasmonic landscape. *Nat Phys* **3**, 477-480, doi:Doi 10.1038/Nphys624 (2007).

25 Wang, K., Schonbrun, E., Steinvurzel, P. & Crozier, K. B. Trapping and rotating nanoparticles using a plasmonic nano-tweezer with an integrated heat sink. *Nat Commun* **2**, doi:Artn 469 Doi 10.1038/Ncomms1480 (2011).

26 Mandal, S., Serey, X. & Erickson, D. Nanomanipulation Using Silicon Photonic Crystal Resonators. *Nano Lett* **10**, 99-104, doi:Doi 10.1021/Nl9029225 (2010).

27 Yang, A. H. J. *et al.* Optical manipulation of nanoparticles and biomolecules in sub-wavelength slot waveguides. *Nature* **457**, 71-75, doi:Doi 10.1038/Nature07593 (2009).

28 Erickson, D., Serey, X., Chen, Y. F. & Mandal, S. Nanomanipulation using near field photonics. *Lab Chip* **11**, 995-1009, doi:Doi 10.1039/C0lc00482k (2011).

29 Joannopoulos, J. D., Meade, R. D. & Winn, J. N. *Photonic crystals : molding the flow of light*. (Princeton University Press, 1995).

30 Graham-Rowe, D. Tunable structural colour. *Nat Photonics* **3**, 551-553, doi:DOI 10.1038/nphoton.2009.172 (2009).

31 Arsenault, A. C., Puzzo, D. P., Manners, I. & Ozin, G. A. Photonic-crystal full-colour displays. *Nat Photonics* **1**, 468-472, doi:DOI 10.1038/nphoton.2007.140 (2007).

32 Walish, J. J., Kang, Y., Mickiewicz, R. A. & Thomas, E. L. Bioinspired Electrochemically Tunable Block Copolymer Full Color Pixels. *Adv Mater* **21**, 3078-+, doi:DOI 10.1002/adma.200900067 (2009).

33 Fudouzi, H. & Xia, Y. N. Colloidal crystals with tunable colors and their use as photonic papers. *Langmuir* **19**, 9653-9660, doi:Doi 10.1021/La034918q (2003).

34 Sirringhaus, H. *et al.* High-resolution inkjet printing of all-polymer transistor circuits. *Science* **290**, 2123-2126, doi:DOI 10.1126/science.290.5499.2123 (2000).

35 Dufresne, E. R. *et al.* Self-assembly of amorphous biophotonic nanostructures by phase separation. *Soft Matter* **5**, 1792-1795, doi:Doi 10.1039/B902775k (2009).

36 Huang, J. Y., Wang, X. D. & Wang, Z. L. Controlled replication of butterfly wings for achieving tunable photonic properties. *Nano Lett* **6**, 2325-2331, doi:Doi 10.1021/Nl061851t (2006).

37 Hanlon, R. T., Cooper, K. M., Budelmann, B. U. & Pappas, T. C. Physiological Color-Change in Squid Iridophores .1. Behavior, Morphology and Pharmacology in Lolliguncula-Brevis. *Cell Tissue Res* **259**, 3-14 (1990).

38 Cooper, K. M., Hanlon, R. T. & Budelmann, B. U. Physiological Color-Change in Squid Iridophores .2. Ultrastructural Mechanisms in Lolliguncula-Brevis. *Cell Tissue Res* **259**, 15-24, doi:Doi 10.1007/Bf00571425 (1990).

39 Blau, S. K. Light as a feather: Structural elements give peacock plumes their color. *Phys Today* **57**, 18-20, doi:Doi 10.1063/1.1650059 (2004).

40 Zi, J. *et al.* Coloration strategies in peacock feathers. *P Natl Acad Sci USA* **100**, 12576-12578 (2003).

41 Parker, A. R., McPhedran, R. C., McKenzie, D. R., Botten, L. C. & Nicorovici, N. A. P. Photonic engineering - Aphrodite's iridescence. *Nature* **409**, 36-37, doi:Doi 10.1038/35051168 (2001).

42 Li, Y. Y. *et al.* Polymer replicas of photonic porous silicon for sensing and drug delivery applications. *Science* **299**, 2045-2047 (2003).

43 Potyrailo, R. A. *et al.* Morpho butterfly wing scales demonstrate highly selective vapour response. *Nat Photonics* **1**, 123-128 (2007).

44 Arsenault, A. C., Miguez, H., Kitaev, V., Ozin, G. A. & Manners, I. A polychromic, fast response metallopolymer gel photonic crystal with solvent and redox tunability: A step towards photonic ink (P-Ink). *Adv Mater* **15**, 503-507 (2003).

45 Kurihara, S. *et al.* Photoswitching properties of photonic band gap material containing azo-polymer liquid crystal. *Eur Polym J* **43**, 4951-4960 (2007).

46 Arsenault, A. C. *et al.* Vapor swellable colloidal photonic crystals with pressure tunability. *J Mater Chem* **15**, 133-138, doi:Doi 10.1039/B410284n (2005).

47 Erickson, D., Rockwood, T., Emery, T., Scherer, A. & Psaltis, D. Nanofluidic tuning of photonic crystal circuits. *Opt Lett* **31**, 59-61, doi:Doi 10.1364/Ol.31.000059 (2006).

48 Fudouzi, H. & Sawada, T. Photonic rubber sheets with tunable color by elastic deformation. *Langmuir* **22**, 1365-1368, doi:Doi 10.1021/La0521037 (2006).

49 Ge, J. P. *et al.* Magnetochromatic Microspheres: Rotating Photonic Crystals. *J Am Chem Soc* **131**, 15687-15694, doi:Doi 10.1021/Ja903626h (2009).

50 Kim, H. *et al.* Structural colour printing using a magnetically tunable and lithographically fixable photonic crystal. *Nat Photonics* **3**, 534-540 (2009).

51 Fudouzi, H. & Xia, Y. N. Photonic papers and inks: Color writing with colorless materials. *Adv Mater* **15**, 892-+, doi:DOI 10.1002/adma.200304795 (2003).

52 Jeong, S. *et al.* Fast and Scalable Printing of Large Area Monolayer Nanoparticles for Nanotexturing Applications. *Nano Lett* **10**, 2989-2994, doi:Doi 10.1021/Nl101432r (2010).

53 Caruso, F. *Colloids and colloid assemblies : synthesis, modification, organization and utilization of colloid particles*. (Wiley-VCH, 2004).

54 Denkov, N. D. *et al.* Mechanism of Formation of 2-Dimensional Crystals from Latex-Particles on Substrates. *Langmuir* **8**, 3183-3190 (1992).

55 Wohlleben, W., Bartels, F. W., Altmann, S. & Leyrer, R. J. Mechano-optical octave-tunable elastic colloidal crystals made from core-shell polymer beads with self-assembly techniques. *Langmuir* **23**, 2961-2969, doi:Doi 10.1021/La062602n (2007).

56 Carlson, R. J. & Asher, S. A. Characterization of Optical Diffraction and Crystal-Structure in Monodisperse Polystyrene Colloids. *Appl Spectrosc* **38**, 297-304, doi:Doi 10.1366/0003702844555548 (1984).

57 Lee, J. N., Park, C. & Whitesides, G. M. Solvent compatibility of poly(dimethylsiloxane)-based microfluidic devices. *Anal Chem* **75**, 6544-6554, doi:Doi 10.1021/Ac0346712 (2003).

58 Miller, R. D. & Jones, T. B. Electro-Orientation of Ellipsoidal Erythrocytes - Theory and Experiment. *Biophys J* **64**, 1588-1595 (1993).

59 Allen, L., Beijersbergen, M. W., Spreeuw, R. J. C. & Woerdman, J. P. Orbital Angular-Momentum of Light and the Transformation of Laguerre-Gaussian Laser Modes. *Phys Rev A* **45**, 8185-8189 (1992).

60 Friese, M. E. J., Enger, J., RubinszteinDunlop, H. & Heckenberg, N. R. Optical angular-momentum transfer to trapped absorbing particles. *Phys Rev A* **54**, 1593-1596 (1996).

61 He, H., Friese, M. E. J., Heckenberg, N. R. & Rubinszteindunlop, H. Direct Observation of Transfer of Angular-Momentum to Absorptive Particles from a Laser-Beam with a Phase Singularity. *Phys Rev Lett* **75**, 826-829 (1995).

62 Vogel, R. *et al.* Synthesis and Surface Modification of Birefringent Vaterite Microspheres. *Langmuir* **25**, 11672-11679, doi:Doi 10.1021/La901532x (2009).

63 Padgett, M. & Bowman, R. Tweezers with a twist. *Nat Photonics* **5**, 343-348, doi:Doi 10.1038/Nphoton.2011.81 (2011).

64 Dholakia, K. & Cizmar, T. Shaping the future of manipulation. *Nat Photonics* **5**, 335-342, doi:Doi 10.1038/Nphoton.2011.80 (2011).

65 La Porta, A. & Wang, M. D. Optical torque wrench: Angular trapping, rotation, and torque detection of quartz microparticles. *Phys Rev Lett* **92**, doi:Artn 190801 Doi 10.1103/Physrevlett.92.190801 (2004).

66 Schneider, C. A., Rasband, W. S. & Eliceiri, K. W. NIH Image to ImageJ: 25 years of image analysis. *Nat Methods* **9**, 671-675, doi:Doi 10.1038/Nmeth.2089 (2012).

67 Chen, Y. F., Serey, X., Sarkar, R., Chen, P. & Erickson, D. Controlled Photonic Manipulation of Proteins and Other Nanomaterials. *Nano Lett* **12**, 1633-1637, doi:Doi 10.1021/Nl204561r (2012).

68 Lin, S. Y., Schonbrun, E. & Crozier, K. Optical Manipulation with Planar Silicon Microring Resonators. *Nano Lett* **10**, 2408-2411, doi:Doi 10.1021/Nl100501d (2010).

69 Juan, M. L., Gordon, R., Pang, Y., Eftekhari, F. & Quidant, R. Self-induced back-action optical trapping of dielectric nanoparticles. *Nat Phys* **5**, 915-919, doi:http://www.nature.com/nphys/journal/v5/n12/suppinfo/nphys1422_S1.html (2009).

70 Wang, K., Schonbrun, E., Steinvurzel, P. & Crozier, K. B. Trapping and rotating nanoparticles using a plasmonic nano-tweezer with an integrated heat sink. *Nat Commun* **2**, 469, doi:http://www.nature.com/ncomms/journal/v2/n9/suppinfo/ncomms1480_S1.html (2011).

71 Liu, M., Zentgraf, T., Liu, Y., Bartal, G. & Zhang, X. Light-driven nanoscale plasmonic motors. *Nat Nano* **5**, 570-573, doi:http://www.nature.com/nnano/journal/v5/n8/abs/nnano.2010.128.html#supplementary-information (2010).

72 Washizu, M., Shikida, M., Aizawa, S. & Hotani, H. Orientation and Transformation of Flagella in Electrostatic-Field. *Ieee T Ind Appl* **28**, 1194-1202 (1992).

73 Minoura, I. & Muto, E. Dielectric measurement of individual microtubules using the electroorientation method. *Biophys J* **90**, 3739-3748, doi:DOI 10.1529/biophysj.105.071324 (2006).

74 Rezakhaniha, R. *et al.* Experimental investigation of collagen waviness and orientation in the arterial adventitia using confocal laser scanning microscopy. *Biomech Model Mechan* **11**, 461-473, doi:DOI 10.1007/s10237-011-0325-z (2012).

75 Serey, X., Mandal, S. & Erickson, D. Comparison of silicon photonic crystal resonator designs for optical trapping of nanomaterials. *Nanotechnology* **21**, doi:305202 10.1088/0957-4484/21/30/305202 (2010).

76 Serey, X., Mandal, S., Chen, Y. F. & Erickson, D. DNA Transport and Delivery in Thermal Gradients near Optofluidic Resonators. *Phys Rev Lett* **108**, doi:Artn 048102 Doi 10.1103/Physrevlett.108.048102 (2012).

77 Tong, L., Miljković, V. D. & Käll, M. Alignment, Rotation, and Spinning of Single Plasmonic Nanoparticles and Nanowires Using Polarization Dependent Optical Forces. *Nano Lett* **10**, 268-273, doi:10.1021/nl9034434 (2009).

78 Han, Y. *et al.* Brownian motion of an ellipsoid. *Science* **314**, 626-630, doi:DOI 10.1126/science.1130146 (2006).

79 Cai, H. & Poon, A. W. Planar optical tweezers using tapered-waveguide junctions. *Opt Lett* **37**, 3000-3002 (2012).

80 Schneider, T. M., Mandre, S. & Brenner, M. P. Algorithm for a Microfluidic Assembly Line. *Phys Rev Lett* **106**, 094503 (2011).

81 Gill, P., Moghadam, T. T. & Ranjbar, B. Differential scanning calorimetry techniques: applications in biology and nanoscience. *J Biomol Tech* **21**, 167-193 (2010).

82 Ivnitski, D., Abdel-Hamid, I., Atanasov, P. & Wilkins, E. Biosensors for detection of pathogenic bacteria. *Biosens Bioelectron* **14**, 599-624, doi:Doi 10.1016/S0956-5663(99)00039-1 (1999).

83 Lazcka, O., Del Campo, F. J. & Munoz, F. X. Pathogen detection: A perspective of traditional methods and biosensors. *Biosens Bioelectron* **22**, 1205-1217, doi:DOI 10.1016/j.bios.2006.06.036 (2007).

84 Leonard, P. *et al.* Advances in biosensors for detection of pathogens in food and water. *Enzyme Microb Tech* **32**, 3-13, doi:Pii S0141-0229(02)00232-6 Doi 10.1016/S0141-0229(02)00232-6 (2003).

85 Turner, A. P. F. Biosensors: sense and sensibility. *Chem Soc Rev* **42**, 3184-3196, doi:Doi 10.1039/C3cs35528d (2013).

86 Day, E. S., Capili, A. D., Borysenko, C. W., Zafari, M. & Whitty, A. Determining the affinity and stoichiometry of interactions between unmodified proteins in solution using Biacore. *Anal Biochem* **440**, 96-107, doi:Doi 10.1016/J.Ab.2013.05.012 (2013).

87 Matsuoka, H. Evanescent wave light scattering - A fusion of the evanescent wave and light scattering techniques to the study of colloids and polymers near the interface. *Macromol Rapid Comm* **22**, 51-67, doi:Doi 10.1002/1521-3927(20010201)22:2<51::Aid-Marc51>3.0.Co;2-5 (2001).

88 Lepage, D., Jimenez, A., Beauvais, J. & Dubowski, J. J. Real-time detection of influenza A virus using semiconductor nanophotonics. *Light-Sci Appl* **2**, doi:UNSP e62 DOI 10.1038/lsa.2013.18 (2013).

89 Patolsky, F. *et al.* Electrical detection of single viruses. *P Natl Acad Sci USA* **101**, 14017-14022, doi:DOI 10.1073/pnas.0406159101 (2004).

90 Saleh, O. A. & Sohn, L. L. Direct detection of antibody-antigen binding using an on-chip artificial pore. *P Natl Acad Sci USA* **100**, 820-824, doi:DOI 10.1073/pnas.0337563100 (2003).

91 Arlett, J. L., Myers, E. B. & Roukes, M. L. Comparative advantages of mechanical biosensors. *Nat Nanotechnol* **6**, 203-215, doi:DOI 10.1038/nnano.2011.44 (2011).

92 Daaboul, G. G. *et al.* High-Throughput Detection and Sizing of Individual Low-Index Nanoparticles and Viruses for Pathogen Identification. *Nano Lett* **10**, 4727-4731, doi:Doi 10.1021/Nl103210p (2010).

93 Wang, S. P. *et al.* Label-free imaging, detection, and mass measurement of single viruses by surface plasmon resonance. *P Natl Acad Sci USA* **107**, 16028-16032, doi:DOI 10.1073/pnas.1005264107 (2010).

94 Chettiar, U. K. & Engheta, N. Internal homogenization: Effective permittivity of a coated sphere. *Opt Express* **20**, 22976-22986 (2012).

95 Capitanio, M. *et al.* Calibration of optical tweezers with differential interference contrast signals. *Rev Sci Instrum* **73**, 1687-1696, doi:Doi 10.1063/1.1460929 (2002).

96 Mullenbroich, M. C., McAlinden, N. & Wright, A. J. Adaptive optics in an optical trapping system for enhanced lateral trap stiffness at depth. *J Optics-Uk* **15**, doi:Artn 075305 Doi 10.1088/2040-8978/15/7/075305 (2013).

97 Erickson, H. P. Size and Shape of Protein Molecules at the Nanometer Level Determined by Sedimentation, Gel Filtration, and Electron Microscopy. *Biol Proced Online* **11**, 32-51, doi:DOI 10.1007/s12575-009-9008-x (2009).

98 Murphy, R. M. *et al.* Size and Structure of Antigen-Antibody Complexes - Electron-Microscopy and Light-Scattering Studies. *Biophys J* **54**, 45-56 (1988).

99 Skottrup, P. D., Nicolaisen, M. & Justesen, A. F. Towards on-site pathogen detection using antibody-based sensors. *Biosens Bioelectron* **24**, 339-348, doi:DOI 10.1016/j.bios.2008.06.045 (2008).

100 Florin, E. L., Pralle, A., Stelzer, E. H. K. & Horber, J. K. H. Photonic force microscope calibration by thermal noise analysis. *Appl Phys a-Mater* **66**, S75-S78, doi:DOI 10.1007/s003390051103 (1998).